

Review

Open Access



Recent progress of sulfide electrolytes for all-solid-state lithium batteries

Han Su[#], Zhao Jiang[#], Yu Liu, Jingru Li, Changdong Gu, Xiuli Wang, Xinhui Xia, Jiangping Tu*

State Key Laboratory of Silicon Materials, Key Laboratory of Advanced Materials and Applications for Batteries of Zhejiang Province, School of Materials Science and Engineering, Zhejiang University, Hangzhou 310000, Zhejiang, China.

*Authors contributed equally.

***Correspondence to:** Prof. Jiangping Tu, State Key Laboratory of Silicon Materials, Key Laboratory of Advanced Materials and Applications for Batteries of Zhejiang Province, School of Materials Science and Engineering, Zhejiang University, No.38, Zheda Road, Hangzhou 310000, Zhejiang, China. E-mail: tujp@zju.edu.cn

How to cite this article: Su H, Jiang Z, Liu Y, Li J, Gu C, Wang X, Xia X, Tu J. Recent progress of sulfide electrolytes for all-solid-state lithium batteries. *Energy Mater* 2022;2:200005. <https://dx.doi.org/10.20517/energymater.2022.01>

Received: 5 Jan 2022 **First Decision:** 7 Feb 2022 **Revised:** 10 Feb 2022 **Accepted:** 18 Feb 2022 **Published:** 28 Feb 2022

Academic Editors: Yuping Wu, Jiazhao Wang **Copy Editor:** Xi-Jun Chen **Production Editor:** Xi-Jun Chen

Abstract

Solid electrolytes are recognized as being pivotal to next-generation energy storage technologies. Sulfide electrolytes with high ionic conductivity represent some of the most promising materials to realize high-energy-density all-solid-state lithium batteries. Due to their soft nature, sulfides possess good wettability against Li metal and their preparation process is relatively effortless. High cell-level sulfide-based all-solid-state lithium batteries have gradually been realized in recent years. However, there are still several disadvantages that sulfide electrolytes need to overcome, including their sensitivity to humid air and instability to electrodes. Herein, the recent progress for sulfide electrolytes, with particular attention given to electrolyte synthesis mechanisms, electrochemical and chemical stability, interphase stabilization and all-solid-state lithium batteries with high cell-level energy density, is presented.

Keywords: Sulfide electrolytes, electrochemical stability, interphase stabilization, all-solid-state lithium batteries

INTRODUCTION

The increasing demand for renewable energy has inevitably resulted in higher requirements for energy storage devices. Rechargeable lithium-ion batteries (LIBs) has played a significant role in large-scale energy storage on account of their high energy density^[1,2]. However, due to the use of liquid organic electrolytes,



© The Author(s) 2022. **Open Access** This article is licensed under a Creative Commons Attribution 4.0 International License (<https://creativecommons.org/licenses/by/4.0/>), which permits unrestricted use, sharing, adaptation, distribution and reproduction in any medium or format, for any purpose, even commercially, as long as you give appropriate credit to the original author(s) and the source, provide a link to the Creative Commons license, and indicate if changes were made.



www.energymaterj.com

combustion, leakage and other safety issues have aroused great concerns^[3,4]. All-solid-state lithium batteries (ASSLBs) employing inorganic solid electrolytes instead of liquid electrolytes can effectively solve this dilemma and as a result have received significant attention^[5].

Inorganic solid electrolytes are essential for ASSLBs^[6,7] and can generally be divided into oxide, sulfide and nitride electrolytes. Among these electrolytes, sulfide electrolytes are considered as some of the most promising candidates because of their high ionic conductivity and suitable mechanical properties^[8,9]. In particular, sulfide-based solid electrolytes that possess higher ionic conductivity than that of liquid electrolytes, such as $\text{Li}_{9.54}\text{Si}_{1.74}\text{P}_{1.44}\text{S}_{11.7}\text{Cl}_{0.3}$ ($2.5 \times 10^{-2} \text{ S cm}^{-1}$), $\text{Li}_{6.6}\text{Si}_{0.6}\text{Sb}_{0.4}\text{S}_5\text{I}$ ($2.4 \times 10^{-2} \text{ S cm}^{-1}$) and $\text{Li}_{6.7}\text{PS}_5\text{ClBr}_{0.7}$ ($2.4 \times 10^{-2} \text{ S cm}^{-1}$), have been developed^[10-12]. Though remarkable progress has been made in recent decades, there are still some challenges for the commercial application of sulfide electrolytes. For instance, they have a narrow electrochemical window, which leads to poor electrochemical compatibility with electrodes^[13,14]. Moreover, sulfide electrolytes have inferior chemical stability to humid air, which results in the generation of toxic H_2S gas, as well as degradation of the electrolytes^[15].

In this review, the recent progress of sulfide electrolytes for ASSLBs is summarized. At first, the synthesis approaches of sulfide electrolytes are discussed systematically. The relationships between the ionic conductivity and crystal structure of sulfide electrolytes are then analyzed, accompanied by a discussion of numerous strategies for improving their ionic conductivity. Moreover, the stability (in terms of electrochemical window and humid air) of sulfide electrolytes is also explored. In particular, the interfacial compatibility between sulfide electrolytes and electrodes (Li metal anodes and oxide cathodes) is described and the corresponding solutions are discussed in detail. The fabrication of thin sulfide electrolyte films for ASSLBs with high cell-lever energy density is also emphasized. Ultimately, we summarize the prospects and consider possible future developments of sulfide electrolytes for ASSLBs.

SYNTHESIS APPROACHES

To date, the synthesis methods of sulfide electrolytes mainly consist of melt-quenching, liquid-phase and mechanical ball-milling approaches.

Melt-quenching approach

Melt quenching is one of the most traditional approaches for the preparation of sulfide glasses. The preparation process involves heating the raw materials at a high temperature and quenching the molten samples in ice water, which is harsh and can easily generate impurities. Minami *et al.*^[16] fabricated $70\text{Li}_2\text{S}\text{-}30\text{P}_2\text{S}_5$ glasses by a melt-quenching technique at different heating temperatures and investigated their local structure. In addition, $70\text{Li}_2\text{S}\text{-}30\text{P}_2\text{S}_5$ glass ceramics were obtained by crystallization of the glasses^[17]. The results showed that the generation of crystalline $\text{Li}_7\text{P}_3\text{S}_{11}$ improved the ionic conductivity of the glass ceramics. However, with increasing heating temperature and holding time, the metastable $\text{Li}_7\text{P}_3\text{S}_{11}$ crystal phase transforms into a thermodynamically stable phase with low ionic conductivity, which decreased the ionic conductivity of the $70\text{Li}_2\text{S}\text{-}30\text{P}_2\text{S}_5$ glass ceramics. Furthermore, by combining the melt-quenching and hot pressing processes, the grain boundaries and pores of the sulfide electrolytes were eliminated, as shown in Figure 1A-C^[18]. As a result, the $\text{Li}_2\text{S}\text{-}\text{P}_2\text{S}_5$ glass-ceramic conductor delivered an enhanced high ionic conductivity of $1.7 \times 10^{-2} \text{ S cm}^{-1}$.

Liquid-phase approach

The developed liquid-phase approach displays large-scale industrial prospects because of its advantages in terms of high efficiency and energy conservation. The raw materials can proceed with a sufficient reaction in solutions and produce homogenous precursors^[19]. Furthermore, liquid-phase approaches have been

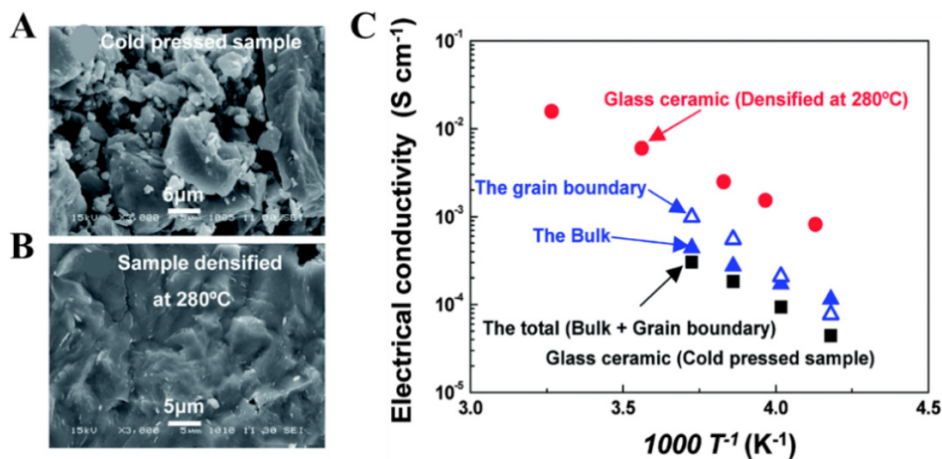


Figure 1. Scanning electron microscopy (SEM) images of $\text{Li}_7\text{P}_3\text{S}_{11}$ glass ceramic from (A) cold-pressed and (B) heat-treated samples. (C) Temperature dependency of the resistances of the glass-ceramic material at different conditions. Reproduced with permission^[18] (Copyright 2014, Royal Society of Chemistry).

employed to enhance the electrode/electrolyte interfacial contact for improving the performance of the batteries^[20]. Nevertheless, residual organic solvents and impurity phases in the samples are inevitable and hinder the transport of Li^+ , resulting in a decrease in the ionic conductivity of the electrolytes and an increase in activation energy^[21]. Li_3PS_4 is the most stable phase in the $\text{Li}_2\text{S}-\text{P}_2\text{S}_5$ system. Liu *et al.*^[22] employed tetrahydrofuran (THF) as a dispersion medium to synthesize Li_3PS_4 . After removing the THF solvent, the obtained β - Li_3PS_4 with a nanoporous structure displayed an ionic conductivity of $1.6 \times 10^{-4} \text{ S cm}^{-1}$ and excellent stability against Li metal^[22]. Ito *et al.*^[21] prepared crystalline $\text{Li}_7\text{P}_3\text{S}_{11}$ by a liquid-phase reaction in a 1,2-dimethoxyethane (DME) organic solvent and its ionic conductivity was $2.7 \times 10^{-4} \text{ S cm}^{-1}$.

Xu *et al.*^[19] applied different organic solvents to synthesize a $\text{Li}_7\text{P}_3\text{S}_{11}$ glass-ceramic electrolyte. THF, acetonitrile (ACN) and THF/ACN mixed solvents were used to prepare a $\text{Li}_7\text{P}_3\text{S}_{11}$ glass ceramic and the corresponding scanning electron microscopy (SEM) images and electrochemical impedance spectroscopy (EIS) analysis of the electrolyte are displayed in Figure 2A-C. It was found that the $\text{Li}_7\text{P}_3\text{S}_{11}$ electrolyte prepared with ACN possessed the highest ionic conductivity ($9.7 \times 10^{-4} \text{ S cm}^{-1}$) and the lowest activation energy (31.2 kJ mol^{-1}) among all the candidates^[19]. In addition, it was reported by Yubuchi *et al.*^[23] that argyrodite-type $\text{Li}_6\text{PS}_5\text{X}$ ($\text{X} = \text{Cl}, \text{Br}$ or I) could also be synthesized with the liquid-phase technique. The $\text{Li}_6\text{PS}_5\text{Cl}$ electrolyte prepared via ethanol displayed an ionic conductivity of $1.4 \times 10^{-5} \text{ S cm}^{-1}$ at room temperature (RT). $\text{Li}_6\text{PS}_5\text{Br}$ with a high ionic conductivity of $3.1 \times 10^{-3} \text{ S cm}^{-1}$ was also synthesized by adopting homogeneous a THF- and ethanol-based solution. Furthermore, solution-processable iodine-based Li-argyrodites with formulas of $\text{Li}_6\text{P}_5\text{SI}$, $\text{Li}_{6.5}\text{P}_{0.5}\text{Ge}_{0.5}\text{S}_5\text{I}$ and $\text{Li}_{6.25}\text{Sn}_{0.25}\text{P}_{0.75}\text{S}_5\text{I}$ were developed by Song *et al.*^[24] in anhydrous ethanol. Among them, the $\text{Li}_{6.5}\text{P}_{0.5}\text{Ge}_{0.5}\text{S}_5\text{I}$ electrolyte showed the highest Li^+ conductivity of $5.4 \times 10^{-4} \text{ S cm}^{-1}$ at RT.

MECHANICAL BALL-MILLING APPROACH

Mechanical ball-milling is a popular approach for synthesizing sulfide electrolytes due to its simple operation. Raw materials undergo mixing, glassification and crystallization during the process of high-energy milling^[25]. Surprisingly, some undiscovered glass materials can be obtained via the ball-milling method^[4]. A 75Li₂S-25P₂S₅ (mol%) glass prepared by mechanical milling showed an ionic conductivity of $3.7 \times 10^{-4} \text{ S cm}^{-1}$ ^[26]. Boulaineau *et al.*^[27] prepared Li-argyrodite $\text{Li}_6\text{PS}_5\text{X}$ ($\text{X} = \text{Cl}, \text{Br}$ or I) by mechanical ball-milling and the ionic conductivity of the synthesized electrolytes could reach a high level of $2-7 \times 10^{-4} \text{ S cm}^{-1}$.

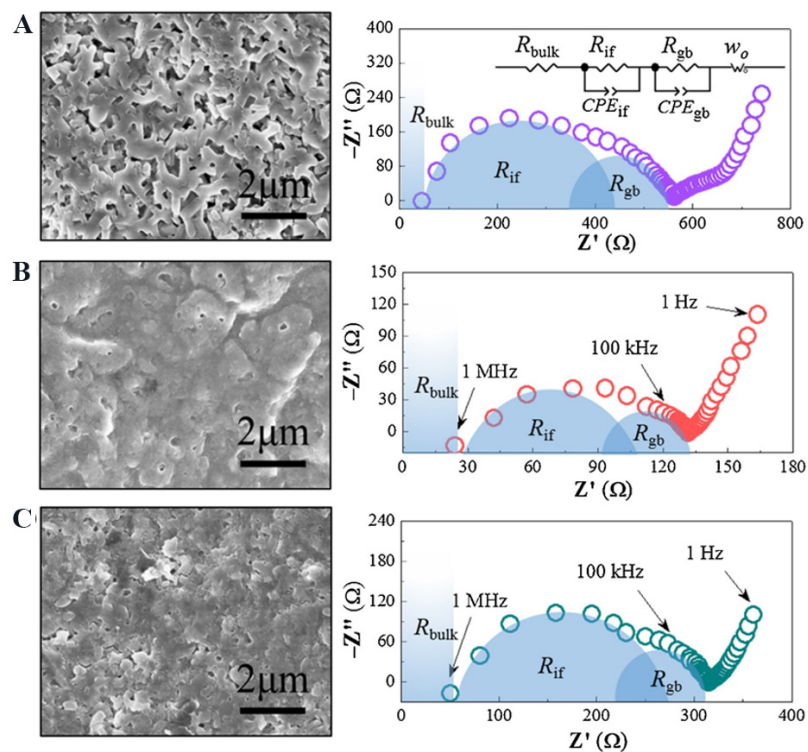


Figure 2. SEM images of $\text{Li}_7\text{P}_3\text{S}_{11}$ pellets prepared by (A) THF, (B) ACN and (C) THF + ACN, and the matching impedance figures at RT. The equivalent circuit is inserted in the impedance spectrum. Reproduced with permission^[19] (Copyright 2016, Elsevier). SEM: Scanning electron microscopy; THF: tetrahydrofuran; ACN: acetonitrile; RT: room temperature.

As described in Figure 3A and B, a $\text{Li}_{\text{e}}\text{PS}_{\text{s}}\text{I}$ ^[28] phase with optimization of the milling time could exhibit a high ionic conductivity of $1.82 \times 10^{-3} \text{ S cm}^{-1}$. To further improve the ionic conductivity of a sulfide electrolyte, the resulting ball-milled materials were annealed. A series of sulfide electrolytes has been developed via mechanical milling plus annealing, including $70\text{Li}_2\text{S}-30\text{P}_2\text{S}_5$ (mol%, $3.2 \times 10^{-3} \text{ S cm}^{-1}$)^[29], $75\text{Li}_2\text{S}-25\text{P}_2\text{S}_5$ (mol%, $5 \times 10^{-4} \text{ S cm}^{-1}$)^[30], $80\text{Li}_2\text{S}-20\text{P}_2\text{S}_5$ (mol%, $7.2 \times 10^{-4} \text{ cm}^{-1}$)^[31], $\text{Li}_{0.54}\text{Si}_{1.74}\text{P}_{1.44}\text{S}_{11.7}\text{Cl}_{0.3}$ ($2.5 \times 10^{-2} \text{ S cm}^{-1}$)^[10], $\text{Li}_{10}\text{SnP}_2\text{S}_{12}$ ($3.8 \times 10^{-3} \text{ S cm}^{-1}$)^[32] and $\text{Li}_{5.5}\text{PS}_{4.5}\text{Cl}_{1.5}$ ($1.2 \times 10^{-2} \text{ S cm}^{-1}$)^[33]. Recently, Liu *et al.*^[34] synthesized a $\text{Li}_{5.6}\text{PS}_{4.6}\text{I}_{1.4}$ glass-ceramic electrolyte using an ultimate-energy mechanical alloying method. As a consequence, S^2/I^- disorder was successfully introduced into the system. The glass-ceramic electrolyte possessed a high ionic conductivity of $2.0 \times 10^{-3} \text{ cm}^{-1}$. However, the ball-milling process is usually tedious and time-consuming, resulting in an increase in production costs. Moreover, the stoichiometric compositions are only uniform over small areas and are inhomogeneous on large scales because the raw materials tend to stick together during the milling process, which may generate impurities^[35].

The selection of preparation methods is a key factor for determining the properties of sulfide electrolytes. The melt-quenching method requires high operating temperatures and is prone to the generation of impurities. In addition, it is difficult to control the crystallinity of the material obtained by the melt-quenching method. However, the melt-quenching method is easy to operate and is well suited to the preparation of glassy sulfide electrolytes. The liquid-phase approach is suitable for large-scale production. Nonetheless, sulfide electrolytes prepared by the liquid-phase method display inferior ionic conductivities, mainly resulting from the existence of residual organic molecules during the preparation process. Mechanical ball-milling approach enables the reaction precursor to be well mixed. Moreover, some glassy sulfides or glass-ceramic sulfides can be obtained by this method. With the post-annealing treatment, the

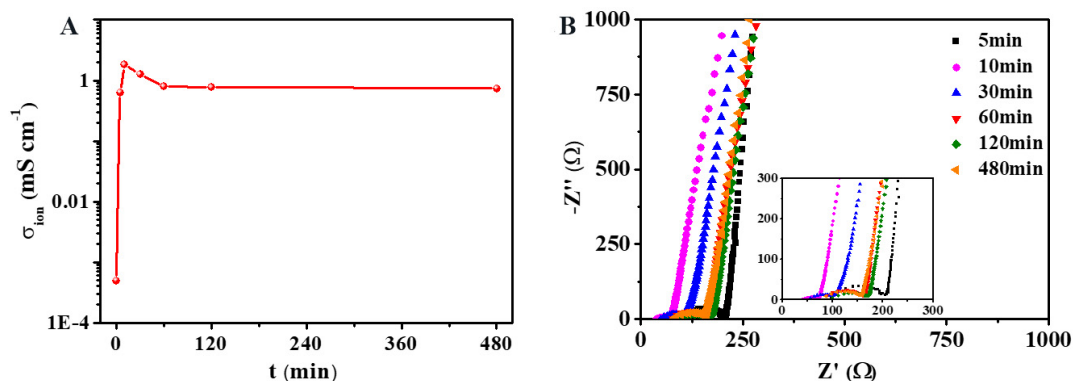


Figure 3. (A) Ionic conductivity (σ) of $\text{Li}_6\text{PS}_5\text{I}$ electrolytes vs. milling time. (B) Nyquist plots of $\text{Li}_6\text{PS}_5\text{I}$ electrolytes for different milling times.^[28] Reproduced with permission^[28] (Copyright 2021, Wiley-VCH).

ionic conductivity and crystallinity of sulfides prepared by the mechanical ball-milling approach will be improved. However, this method is not practical for realistic production. The ionic conductivities of representative sulfide electrolytes prepared by different methods are displayed in Table 1.

STRUCTURE AND CONDUCTIVITY OF SULFIDE ELECTROLYTES

Research into sulfide-based electrolytes can be traced back to 1981 with the $\text{Li}_2\text{S}-\text{P}_2\text{S}_5$ system^[36]. After considerable efforts, the ionic conductivity of sulfide electrolytes can now match or exceed that of liquid organic electrolytes^[10,51]. In this section, the relationship between the structure and ionic conductivity of sulfides, including glasses and glass ceramics, thio-LISICONs, $\text{Li}_{11-x}\text{M}_{2-x}\text{P}_{1+x}\text{S}_{12}$ ($\text{M} = \text{Ge}, \text{Sn}$ or Si) compounds and $\text{Li}_6\text{PS}_5\text{X}$ ($\text{X} = \text{Cl}, \text{Br}$ or I) argyrodites, is reviewed. A detailed summary of the ionic conductivities and activation energies of sulfide electrolytes with the corresponding structures is presented in Table 2.

Sulfide glasses

The conduction pathways of sulfide glasses are isotropic and the grain boundary resistances are easy to eliminate. Therefore, sulfide glasses are generally considered to possess higher ionic conductivity than their corresponding crystalline materials. A detailed investigation of $x\text{Li}_2\text{S}-(100-x)\text{P}_2\text{S}_5$ (mol%) binary systems with different Li_2S fractions was carried out by Dietrich *et al.*^[62] and Hayashi *et al.*^[45] The results showed a single glass phase can form between $x = 0.4$ and 0.8 . Furthermore, the relationship between the local structure of the thiophosphate building blocks and the ionic conductivity was revealed in their work. As represented in Figure 4, a continuous change can be observed from dominant di-tetrahedral $\text{P}_2\text{S}_7^{4-}$ to mono-tetrahedral PS_4^{3-} with increasing Li_2S content. The 75Li₂S-25P₂S₅ glass material with only PS_4^{3-} tetrahedra delivered the highest ionic conductivity of $2.8 \times 10^{-4} \text{ S cm}^{-1}$ at RT. Moreover, $x\text{Li}_2\text{S}-(100-x)\text{SiS}_2$ and $x\text{Li}_2\text{S}-(100-x)\text{B}_2\text{S}_3$ glass materials with wide composition ranges have been reported with ionic conductivities of $\sim 10^{-4} \text{ S cm}^{-1}$ ^[63,64].

Doping lithium salts into glass electrolytes is a common method to enhance the Li^+ carrier concentration and thus improve the ionic conductivity of glasses. The addition of small amounts of Li_xMO_y (e.g., Li_4SiO_4 , Li_3BO_3 , Li_3GeO_4 and Li_3PO_4) in $x\text{Li}_2\text{S}-(100-x)\text{SiS}_2$ glass materials can enhance their stability against crystallization and maintain the level of ionic conductivity at $\sim 10^{-3} \text{ S cm}^{-1}$ ^[65,66]. In addition, LiX ($\text{X} = \text{Cl}, \text{Br}$ or I) is usually applied to enhance the ionic conductivity of glasses. For instance, the $\text{Li}_2\text{S}-\text{B}_2\text{S}_3-\text{LiI}$ and $\text{Li}_2\text{S}-\text{SiS}_2-\text{LiI}$ systems presented ionic conductivities of 1.7×10^{-3} and $1.8 \times 10^{-3} \text{ S cm}^{-1}$, respectively^[67,68]. In contrast, the addition of lithium halides narrows the electrochemical stability window of glass materials because of their decomposition. Furthermore, with LiBH_4 as a doping agent, the $\text{Li}_2\text{S}-\text{B}_2\text{S}_3-\text{LiBH}_4$ system

Table 1. Ionic conductivities of representative sulfide electrolytes prepared by different methods

Material	Conductivity (S cm^{-1})*	Preparation method	Ref.
70Li ₂ S-30P ₂ S ₅ glass	9.2×10^{-5}	Melt quenching	[16]
Li ₂ S-P ₂ S ₅ -LiI glass	$\sim 10^{-3}$	Melt quenching	[36]
70Li ₂ S-30P ₂ S ₅ glass	8.0×10^{-5}	Melt quenching	[18]
β -Li ₃ PS ₄	1.6×10^{-4}	Liquid phase (THF)	[22]
Li ₃ PS ₄	2.3×10^{-6}	Liquid phase (N-methylformamide)	[37]
Li ₃ PS ₄	3.3×10^{-4}	Liquid phase (ethyl acetate)	[38]
Li ₇ P ₃ S ₁₁	1.0×10^{-3}	Liquid phase (ACN)	[39]
Li ₇ P ₃ S ₁₁	2.7×10^{-4}	Liquid phase (DME)	[21]
Li ₇ P ₃ S ₁₁	9.7×10^{-4}	Liquid phase (ACN/THF/CAN + THF)	[19]
Li ₇ P ₃ S ₁₁	8.7×10^{-4}	Liquid phase (ACN)	[40]
Li ₆ PS ₅ Cl	1.4×10^{-5}	Liquid phase (ethanol)	[41]
Li ₆ PS ₅ Cl	6.0×10^{-5}	Liquid phase (ethanol and ethyl acetate)	[42]
Li ₆ PS ₅ Cl	2.4×10^{-3}	Liquid phase (THF and ethanol)	[43]
Li ₆ PS ₅ Br	1.9×10^{-4}	Liquid phase (ethanol)	[23]
Li ₆ PS ₅ Br	3.9×10^{-3}	Liquid phase (THF and ethanol)	[44]
Li _{5.5} PS _{4.5} Cl _{1.5}	3.9×10^{-3}	Liquid phase (THF and ethanol)	[43]
Amorphous Li ₃ PS ₄	2.0×10^{-4}	High-energy ball milling	[45]
Li ₃ PS ₄	1.0×10^{-3}	Mechanical milling	[46]
Li ₇ P ₃ S ₁₁	3.2×10^{-3}	Mechanical milling	[47]
Li ₆ PS ₅ Cl	6.2×10^{-4}	High-energy ball milling	[27]
Li ₆ PS ₅ I	1.9×10^{-4}	High-energy ball milling	[27]
Li _{6.24} P _{0.823} Sn _{0.177} S _{4.58} I _{0.9}	3.5×10^{-4}	High-energy ball milling	[48]
Li _{5.5} PS _{4.5} Cl _{1.5}	1.0×10^{-2}	Ultimate-energy mechanical alloying	[25]
Li ₆ PS ₅ I	7.9×10^{-4}	Ultimate-energy mechanical alloying	[28]
Li _{5.6} PS _{4.6} I _{1.4}	2.0×10^{-3}	Ultimate-energy mechanical alloying	[34]
Li ₂ S-P ₂ S ₅ -Li ₃ N glass	5.8×10^{-4}	Mechanical milling	[26]
Li ₂ S-P ₂ S ₅ -Li ₃ N glass ceramic	1.4×10^{-3}	Mechanical milling	[26]
Li ₁₀ Ge(P _{0.925} Sb _{0.075}) ₂ S ₁₂	1.7×10^{-2}	Mechanical milling	[49]
Li ₁₀ SnP ₂ S ₁₂	3.2×10^{-3}	Mechanical milling	[50]

*Unless otherwise specified, the ionic conductivity is tested at RT. THF: Tetrahydrofuran; ACN: acetonitrile; DME: 1,2-dimethoxyethane; RT: room temperature.

delivered a high ionic conductivity of $1.6 \times 10^{-3} \text{ S cm}^{-1}$ and a stable electrochemical window up to 5 V^[69].

Sulfide glass ceramics

Glass ceramics consist of amorphous and crystalline phases, which are usually prepared through heat treatment of the glass phase. The types of crystals formed depend on the composition of the glass and the conditions of the heat treatment. Currently, research into glass-ceramic electrolytes is mainly focused on the Li₂S-P₂S₅ system. Different crystalline phases are generated in $x\text{Li}_2\text{S}-(100-x)\text{P}_2\text{S}_5$ (mol%) glass materials depending on the x value, as displayed in Figure 5^[70]. For instance, at $x < 70$ mol%, the formation of Li₂P₂S₆ or Li₄P₂S₆ phases with low ionic conductivity decreases the overall conductivity of the glass ceramic^[71,72]. However, for $x \geq 70$ mol%, the crystalline phases of Li_{3.25}P_{0.95}S₄ and Li₇P₃S₁₁ with high ionic conductivity precipitate in the glass materials and significantly increase the ionic conductivity^[29,31,73]. Very recently, a high-energy ball-milling method was utilized to produce glass-ceramic electrolytes in a one-pot process. The prepared glass ceramics displayed an ionic conductivity of $\sim 10^{-3} \text{ S cm}^{-1}$ ^[27,34,74].

Table 2. Ionic conductivities of representative sulfide electrolytes and the corresponding structures

Material	Structure	Conductivity (S cm^{-1})*	E_a (eV)	Ref.
Li_3PS_4	Glass	2.0×10^{-4}	0.35	[45]
0.4LiI-0.6Li ₄ SnS ₄	Glass	4.1×10^{-4} (30 °C)	0.43	[52]
Li ₂ S-P ₂ S ₅ -LiI	Glass	$\sim 10^{-3}$	0.30	[36]
Li ₇ P ₃ S ₁₁	Glass ceramic	1.7×10^{-2}	0.18	[18]
Li ₇ P _{2.9} Sb _{0.1} S _{10.75} O _{0.25}	Glass ceramic	1.6×10^{-3}	0.28	[53]
Li _{5.6} PS _{4.6} I _{1.4}	Glass ceramic	2.0×10^{-3}	0.31	[34]
Li _{6.5} In _{0.25} P _{0.75} S ₅ I	Glass ceramic	1.0×10^{-3}	0.28	[28]
Li ₇ Ag _{0.1} P ₃ S ₁₁ I _{0.1}	Triclinic	1.3×10^{-3}	0.23	[54]
Li _{9.6} P ₃ S ₁₂	Tetragonal	1.2×10^{-3}	0.26	[10]
Li ₄ SnS ₄	Orthorhombic	7.0×10^{-5}	0.41	[55]
Li _{3.334} Ge _{0.334} As _{0.666} S ₄	Orthorhombic	1.1×10^{-3}	0.17	[56]
Li _{3.25} Ge _{0.25} P _{0.75} S ₄	Monoclinic	2.2×10^{-3}	0.21	[57]
Li ₁₀ GeP ₂ S ₁₂	Tetragonal	1.2×10^{-2}	0.25	[51]
Li ₁₀ SnP ₂ S ₁₂	Tetragonal	4.0×10^{-3} (27 °C)	0.27	[58]
Li ₁₀ SiP ₂ S ₁₂	Tetragonal	2.0×10^{-3} (27 °C)	0.30	[59]
Li ₁₀ Si _{0.3} Sn _{0.7} P ₂ S ₁₂	Tetragonal	8.0×10^{-3}	0.29	[59]
Li ₁₀ Ge(P _{0.925} Sb _{0.075}) ₂ S ₁₂	Tetragonal	1.7×10^{-2}	0.27	[49]
Li _{5.5} PS _{4.5} Cl _{1.5}	Cubic	9.4×10^{-3}	0.29	[33]
Li _{6.7} Si _{0.7} Sb _{0.3} S ₅ I	Cubic	1.1×10^{-2}	0.26	[11]
Li _{5.3} PS _{4.3} ClBr _{0.7}	Cubic	2.4×10^{-2}	0.155	[12]
Li _{6.25} PS _{4.75} N _{0.25} Cl	Cubic	1.5×10^{-3}	0.26	[60]
Li _{6.3} P _{0.7} Sn _{0.3} S _{4.4} O _{0.6} I	Cubic	2.3×10^{-4} (30 °C)	0.32	[61]

*Unless otherwise specified, the ionic conductivity is tested at room temperature.

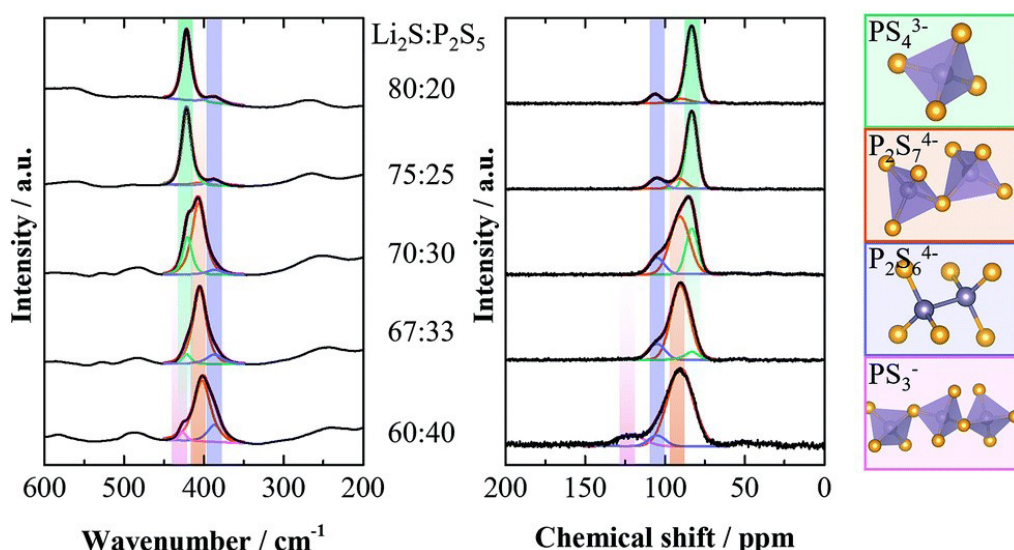


Figure 4. Raman and ^{31}P magic angle spinning-nuclear magnetic resonance (MAS-NMR) spectra of $x\text{Li}_2\text{S}-(100-x)\text{P}_2\text{S}_5$ glasses with different Li_2S contents. Reproduced with permission^[62] (Copyright 2017, Royal Society of Chemistry).

Nonetheless, the appearance of the crystallization region leads to an increase in the grain boundary impedance. To improve the conductivities of glass-ceramic materials, Seino *et al.*^[18] performed a hot-pressing process to eliminate the grain boundaries in 70Li₂S-30P₂S₅ glass ceramics. The obtained electrolytes

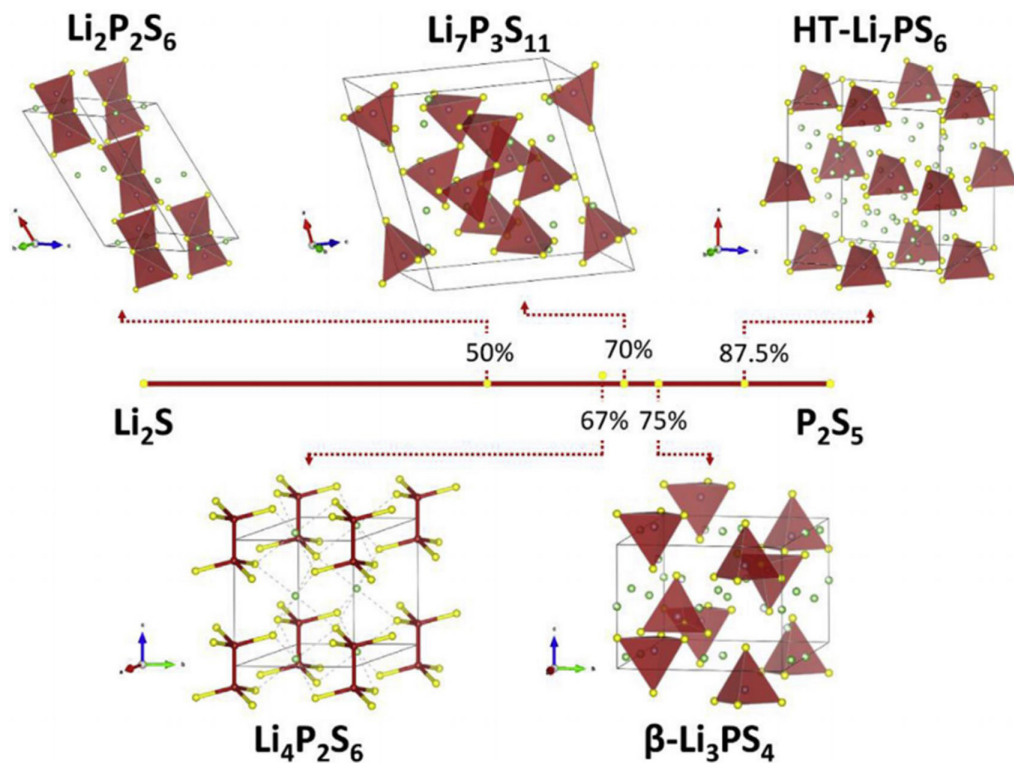


Figure 5. Different crystalline phases generated within the Li_2S - P_2S_5 binary system. Reproduced with permission^[70] (Copyright 2018, Elsevier).

showed a superior conductivity of $1.7 \times 10^{-2} \text{ S cm}^{-1}$. In addition, a doping strategy was used to enhance the ionic conductivity of glass ceramics. It was reported by Xu *et al.*^[35] that replacing P^{5+} with Mo^{4+} ions could not only generate point defects to improve the ionic conductivity but also broaden the Li^+ transport channels. As a consequence, the Mo-doped 70 Li_2S -30 P_2S_5 glass-ceramic electrolyte represented a high ionic conductivity of $4.8 \times 10^{-3} \text{ S cm}^{-1}$ ^[35]. Mn and I co-doping was also applied in their later work to optimize the $\text{Li}_7\text{P}_3\text{S}_{11}$ glass ceramic. The prepared $\text{Li}_{7.9}\text{Mn}_{0.1}\text{S}_{10.7}\text{I}_{0.3}$ glass-ceramic electrolyte possessed a high ionic conductivity ($5.6 \times 10^{-3} \text{ S cm}^{-1}$) and a wide electrochemical window (up to 5 V)^[75].

SULFIDE CRYSTALLINE ELECTROLYTES

Thio-LISICONs

The thio-LISICON structures found in the Li_2S - GeS_2 , Li_2S - GeS_2 - Ga_2S_3 and Li_2S - GeS_2 - ZnS systems were derived from a LISICON-type γ - Li_3PO_4 electrolyte by replacing O with S^[76]. S possesses lower electronegativity and a larger radius than O, and is therefore capable of reducing the Li^+ binding energy and broadening the Li^+ migration channels. Therefore, thio-LISICON electrolytes are expected to have higher ionic conductivity than oxide electrolytes^[13,51]. Six materials [Li_4GeS_4 , Li_2GeS_3 , $\text{Li}_2\text{ZnGeS}_4$, $\text{Li}_{4-2x}\text{Zn}_x\text{GeS}_4$, Li_5GaS_4 and $\text{Li}_{4+x+\delta}(\text{Ge}_{1-\delta-x}\text{Ga}_x)\text{S}_4$] were discovered by Kanno *et al.*^[76] to possess the thio-LISICON structure. Among these thio-LISICON electrolytes, orthorhombic $\text{Li}_{4+x+\delta}(\text{Ge}_{1-\delta-x}\text{Ga}_x)\text{S}_4$ exhibited the highest ionic conductivity of $6.5 \times 10^{-5} \text{ S cm}^{-1}$ at RT. The orthorhombic Li_4GeS_4 electrolyte displayed a low ionic conductivity ($2.0 \times 10^{-7} \text{ S cm}^{-1}$) at RT^[76], while the Li_4GeS_4 thin film was discovered to possess a high ionic conductivity of $7.5 \times 10^{-5} \text{ S cm}^{-1}$ ^[77]. Moreover, the Li_4SnS_4 electrolyte, possessing an ionic conductivity of $7.5 \times 10^{-5} \text{ S cm}^{-1}$, is also defined as thio-LISICON. Furthermore, with As or Sb aliovalent doping, $\text{Li}_{3.833}\text{Sn}_{0.833}\text{As}_{0.166}\text{S}_4$ and $\text{Li}_{3.85}\text{Sn}_{0.85}\text{Sb}_{0.15}\text{S}_4$ electrolytes showed enhanced ionic conductivities of 1.4×10^{-3} and $8.5 \times 10^{-4} \text{ S cm}^{-1}$, respectively^[78,79].

A more detailed investigation of the thio-LISICON structure was carried out for the $\text{Li}_2\text{S}-\text{GeS}_2-\text{P}_2\text{S}_5$ system. Kanno *et al.*^[57] obtained $\text{Li}_{4-x}\text{Ge}_{1-x}\text{P}_x\text{S}_4$ ($0 < x < 1$) by partial substituting Ge^{4+} with P^{5+} in the Li_4GeP_4 electrolyte. The aliovalent P doping could introduce lithium vacancies into the crystal structure to improve the ionic conductivity significantly. As displayed in **Figure 6A** and **B**, the crystal structure is based on the parent structure of Li_4GeS_4 . The X-ray diffraction (XRD) pattern illustrated that $\text{Li}_{4-x}\text{Ge}_{1-x}\text{P}_x\text{S}_4$ ($0 < x < 1$) electrolytes could be regarded as a solid solution between $\gamma\text{-Li}_3\text{PS}_4$ and Li_4GeS_4 ^[2]. According to the appearance of superlattice reflections, the $\text{Li}_{4-x}\text{Ge}_{1-x}\text{P}_x\text{S}_4$ ($0 < x < 1$) system can be divided into three types, namely, the orthorhombic thio-LISICON I region ($0 < x \leq 0.6$), the monoclinic thio-LISICON II region ($0.6 < x < 0.8$) and monoclinic thio-LISICON III region ($0.8 \leq x < 1$). Among these regions, the $\text{Li}_{3.25}\text{P}_{0.75}\text{Ge}_{0.25}\text{S}_4$ electrolyte in the thio-LISICON II region displayed the highest ionic conductivity of $2.2 \times 10^{-3} \text{ S cm}^{-1}$ ^[57]. Furthermore, Nishino *et al.*^[80] evaluated the activation energy and the diffusion coefficient of $\text{Li}_{4-x}\text{Ge}_{1-x}\text{P}_x\text{S}_4$ thio-LISICON by long-time quantum molecular dynamics simulations. The lithium vacancies or excess lithium atoms from doping triggered a new diffusion pathway and drastically decreased the activation energy through the lithium vacancy or interstitial mechanism^[80]. Various LiSiCON (oxide) and thio-LISICON (sulfide) materials with their conduction mechanisms and ionic conductivities are summarized in **Figure 7**^[57].

$\text{Li}_{11-x}\text{M}_{2-x}\text{P}_{1+x}\text{S}_{12}$ ($\text{M} = \text{Ge, Sn or Si}$)

In order to achieve ASSLBs with high energy density, it is essential to develop a sulfide electrolyte with ultrahigh ionic conductivity. The tetragonal $\text{Li}_{10}\text{GeP}_2\text{S}_{12}$ (LGPS) electrolyte with a brand-new three-dimensional (3D) framework structure was reported by Kamaya *et al.*^[51] in 2011. LGPS is the first sulfide electrolyte that exhibits an extremely high ionic conductivity ($1.2 \times 10^{-2} \text{ S cm}^{-1}$) comparable to that of liquid organic electrolytes. As exhibited in **Figure 8**, the ternary LGPS electrolyte is composed of $(\text{Ge}_{0.5}\text{P}_{0.5})\text{S}_4$ tetrahedra, PS_4 tetrahedra, LiS_4 tetrahedra and LiS_6 octahedra. The $(\text{Ge}_{0.5}\text{P}_{0.5})\text{S}_4$ tetrahedra and LiS_6 octahedra form a one-dimensional (1D) Li^+ conduction framework along the c axis by sharing a common edge. These 1D chains are interconnected via PS_4 tetrahedra, which share a common corner with the LiS_6 octahedra. Furthermore, the 1D Li^+ conduction channel consists of LiS_4 tetrahedra sharing a common edge in the 16h and 8f sites^[51].

It was speculated that the Li ions in LGPS migrate through 1D diffusion pathways along the c axis. However, further investigation into the LGPS electrolyte by advanced characterization techniques and density functional theory (DFT) calculations overturned this suggestion. A variety of complementary techniques were employed by Kuhn *et al.*^[81] to characterize the structure and Li^+ dynamics of the LGPS electrolyte. No strong anisotropic signs of diffusivity were found in the material. Therefore, it was concluded that the exceptionally high ionic conductivity of LGPS electrolyte should be attributed to nearly isotropic Li hopping processes in the bulk lattice with an E_a value of $\sim 0.22 \text{ eV}$ ^[81]. Also, it was demonstrated by Mo *et al.*^[82] that the LGPS electrolyte is a 3D conductor rather than a 1D conductor. The reason is that 1D conductors cannot maintain good conductivity due to inevitable channel blocking defects. Thus, some crossover between 1D channels is required to bypass these defects^[83].

Unfortunately, the high cost of Ge raw materials hinders the application of the LGPS electrolyte. Replacing Ge with low-cost elements (e.g., Sn or Si) is an effective approach to reduce the production costs of LGPS. A $\text{Li}_{10}(\text{Ge}_{1-x}\text{M}_x)\text{P}_2\text{S}_{12}$ ($\text{M} = \text{Sn or Si}$) mixed cation system was synthesized by Kato *et al.*^[84] to evaluate the effect of Sn and Si substitution. It was found that Sn and Si substitution reduces the ionic conductivity of the system, indicating that the lattice volume is not the only factor that affects the ionic conductivity^[84]. The Sn analog $\text{Li}_{10}\text{SnP}_2\text{S}_{12}$ electrolyte displayed an ionic conductivity of $7 \times 10^{-3} \text{ S cm}^{-1}$, in good agreement with theoretical calculations. The $\text{Li}_{10}\text{SiP}_2\text{S}_{12}$ electrolyte was expected to possess an enhanced ionic conductivity ($2.3 \times 10^{-2} \text{ S cm}^{-1}$) and lower activation energy (0.20 eV) compared to the pristine LGPS electrolyte according

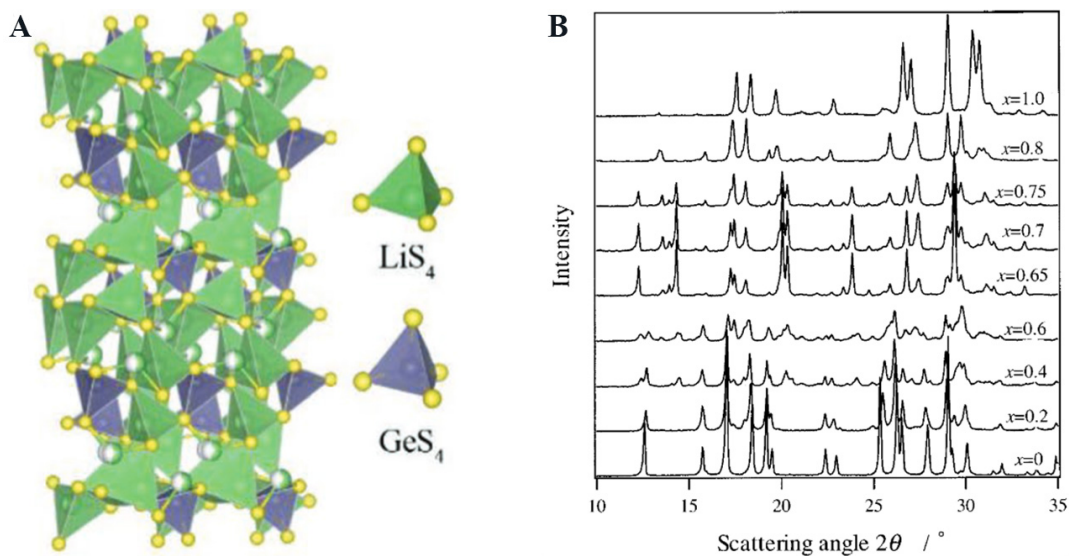


Figure 6. (A) Structure of thio-LISICON based on the parent structure of Li_4GeS_4 . (B) XRD patterns of $\text{Li}_{4-x}\text{Ge}_{1-x}\text{P}_x\text{S}_4$. Reproduced with permission^[2] (Copyright 2019, Wiley-VCH). XRD: X-ray diffraction.

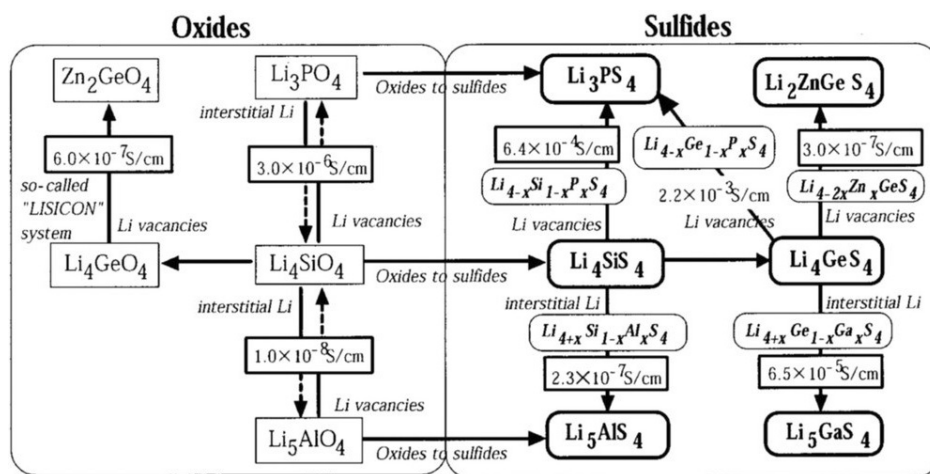


Figure 7. LISICON and thio-LISICON family maps with listed lithium-ion conduction mechanisms and ionic conductivity values. Reproduced with permission^[57] (Copyright 2001, Electrochemical Society).

to theoretical calculations^[85]. However, the experiment results demonstrated that crystalline $\text{Li}_{10}\text{SiP}_2\text{S}_{12}$ only has a low ionic conductivity of $2.3 \times 10^{-3} \text{ S cm}^{-1}$ ^[86]. The reason behind this contradiction has not yet been revealed. Furthermore, in the LGPS family, two newly prepared electrolytes, namely, $\text{Li}_{10.35}\text{Si}_{1.35}\text{P}_{1.65}\text{S}_{12}$ and $\text{Li}_{9.54}\text{Si}_{1.74}\text{P}_{1.44}\text{S}_{11.7}\text{Cl}_{0.3}$, exhibit ultrahigh ionic conductivities of 2.0×10^{-2} and $2.5 \times 10^{-2} \text{ S cm}^{-1}$, respectively^[10,87].

$\text{Li}_6\text{PS}_5\text{X}$ ($\text{X} = \text{Cl}, \text{Br}$ or I)

Ag_8GeS_6 is the first known solid electrolyte with an argyrodite structure (space group $\text{F}4\bar{3}\text{m}$). The Ag_8GeS_6 electrolyte has a high ionic conductivity and mobility of Ag^+ ions due to its highly disordered cation arrangements^[88]. The Ag^+ ions in this electrolyte can be substituted by Cu^+ ions and the argyrodite structure is still maintained^[89]. Considering that the ionic radii of Li^+ (73 ppm) and Cu^+ (74 ppm) are similar, $\text{Li}_6\text{PS}_5\text{X}$ ($\text{X} = \text{Cl}, \text{Br}$ or I) electrolytes were proposed by substituting Cu^+ with Li^+ and substituting Ge^{4+} with P^{5+} and $\text{X}^{[88]}$. In the $\text{Li}_6\text{PS}_5\text{X}$ ($\text{X} = \text{Cl}, \text{Br}$ or I) system, three different jump processes occur, including doublet jumps

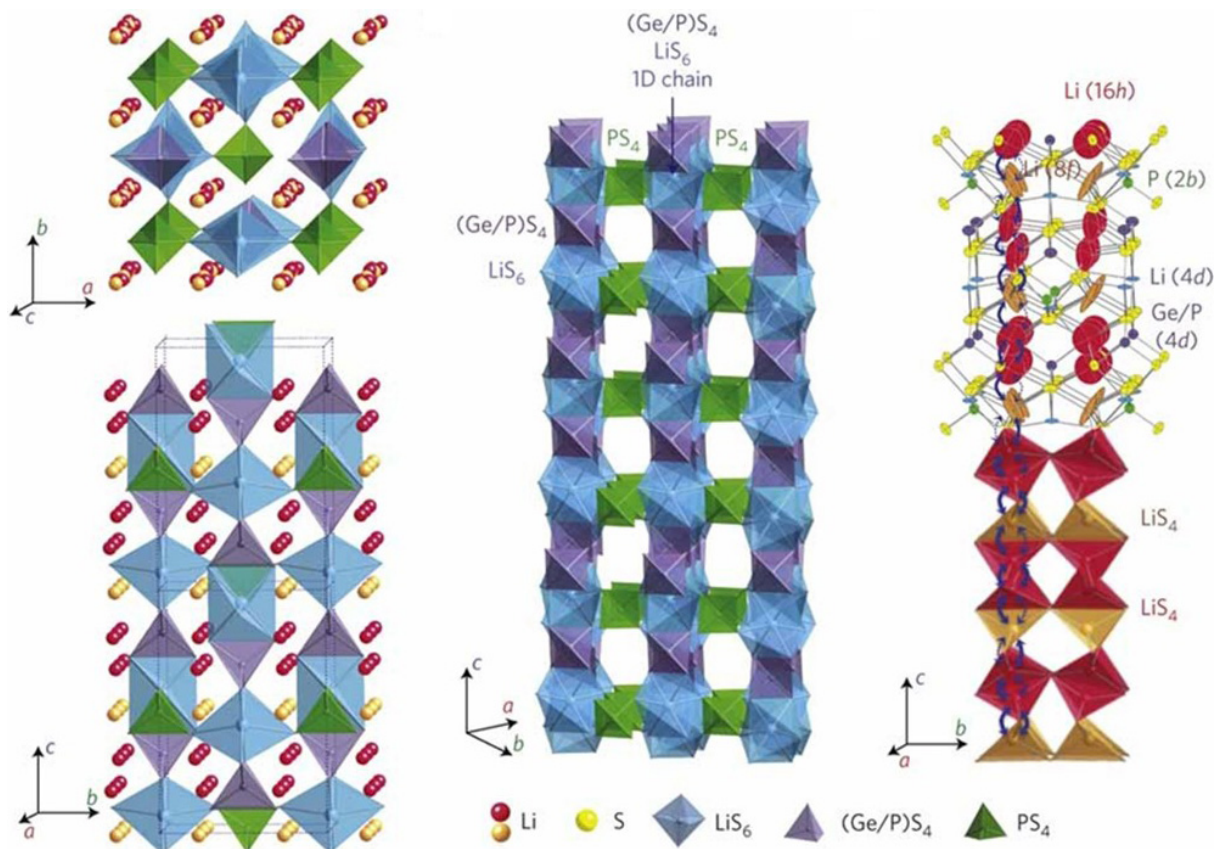


Figure 8. Crystal structure of $\text{Li}_{10}\text{GeP}_2\text{S}_{12}$. Reproduced with permission^[51] (Copyright 2011, Springer Nature Publishing AG).

(48 h-24 g-48 h), intracage jumps (48 h-48 h) and intercage jumps, as shown in **Figure 9A** and **B**^[90]. It was demonstrated by de Klerk *et al.*^[91] that the intercage jumps dominate long-range Li^+ transport and the site disorder between the 4a and 4c sites has a significant impact on the ionic conductivity. The argyrodite-type electrolytes $\text{Li}_6\text{PS}_5\text{Cl}$, $\text{Li}_6\text{PS}_5\text{Br}$ and $\text{Li}_6\text{PS}_5\text{I}$ exhibited ionic conductivities of 1.9×10^{-3} , 6.8×10^{-4} and $4.6 \times 10^{-7} \text{ S cm}^{-1}$, respectively^[92].

Numerous studies have shown that the differences in ionic conductivity in argyrodite-type electrolytes originate from the different degrees of S^{2-}/X^- anion disorder. In $\text{Li}_6\text{PS}_5\text{Cl}$ and $\text{Li}_6\text{PS}_5\text{Br}$, the S^{2-} and Cl^- , or S^{2-} and Br^- ions, at the 4a and 4c sites are partially disordered because of their relatively close ionic radii^[93]. However, the large I^- ions can only occupy the 4a sites and are not able to swap with S^{2-} ions at the 4c site, thus resulting in a fully ordered anion framework^[94]. The $\text{Li}_6\text{PS}_5\text{Cl}$ and $\text{Li}_6\text{PS}_5\text{Br}$ electrolytes with various S^{2-}/X^- anion-site disorders were investigated by first-principles molecular dynamics calculations. It was found by Morgan *et al.*^[95] that the degree of S^{2-}/X^- anion disorder determines the diffusion pathways of the active Li^+ . For anion-ordered systems, the lithium motion is restricted and orbits around the S positions because the critical site-site pathways are inactive and disconnected. In contrast, for anion-disordered systems, the active site-site pathways can form a 3D diffusion network, which enables the long-range diffusion of Li^+ ^[95].

Therefore, considerable efforts have been made to improve the ionic conductivity by increasing the degree of site disorder. It was discovered by Zhao *et al.*^[48] that replacing P^{5+} with larger cations not only broadens the unit cell but also induces site disorder, which is conducive to the transport of Li^+ . By substituting Sn, the

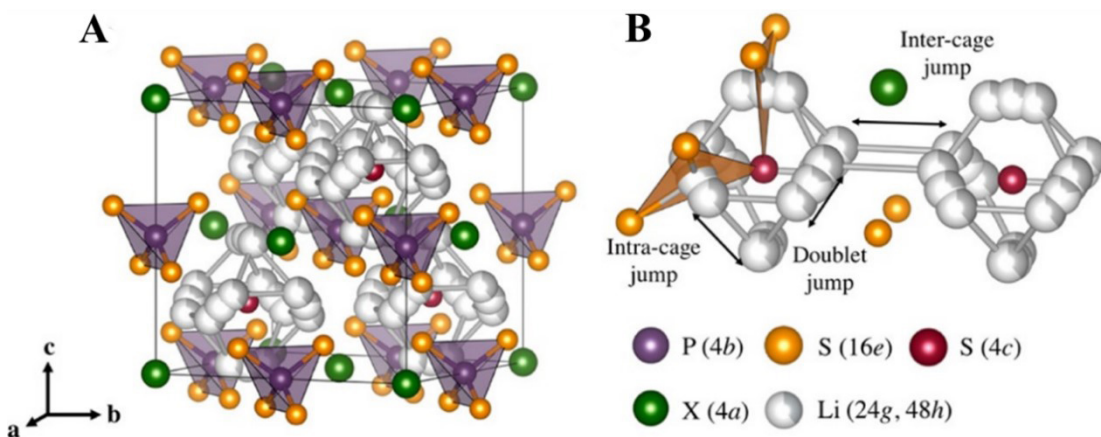


Figure 9. (A) Crystal structure of $\text{Li}_6\text{PS}_5\text{X}$ (X = Cl, Br or I). (B) Li positions forming localized cages in which multiple jump processes are possible. Reproduced with permission^[90] (Copyright 2017, American Chemical Society).

optimized $\text{Li}_{0.24}\text{P}_{0.823}\text{Sn}_{0.177}\text{S}_{4.58}\text{I}_{0.9}$ electrolyte delivered a high ionic conductivity of $3.5 \times 10^{-4} \text{ S cm}^{-1}$, which was 125 times higher than that of the pristine $\text{Li}_6\text{PS}_5\text{I}$ electrolyte^[48]. The influence of Ge substitution on $\text{Li}_{6+x}\text{P}_{1-x}\text{Ge}_x\text{S}_5\text{I}$ electrolytes was also systematically explored by Kraft *et al.*^[90]. The anion site disorder could be induced by the substitution of Ge. As a result, the $\text{Li}_{0.6}\text{P}_{0.4}\text{Ge}_{0.6}\text{S}_5\text{I}$ electrolytes displayed an ionic conductivity of $5.4 \times 10^{-3} \text{ S cm}^{-1}$ after cold-pressing and $1.84 \times 10^{-2} \text{ S cm}^{-1}$ after sintering at 298 K^[96]. A three-fold increase in the ionic conductivity of the $\text{Li}_{0.35}\text{P}_{0.65}\text{Si}_{0.35}\text{S}_5\text{Br}$ electrolyte could be observed compared to that of the unsubstituted sample.^[97]

Furthermore, increasing the halogen content in $\text{Li}_6\text{PS}_5\text{X}$ (X = Cl, Br or I) electrolytes can also effectively improve the anion disorder and enhance their ionic conductivity^[34,98,99]. The argyrodite $\text{Li}_{5.3}\text{PS}_{4.3}\text{Cl}_{1.7}$ and $\text{Li}_{5.3}\text{PS}_{4.3}\text{Br}_{1.7}$ electrolytes have ionic conductivities of 1.7×10^{-2} and $1.1 \times 10^{-2} \text{ S cm}^{-1}$ upon sintering, respectively^[98,99]. Recently, Patel *et al.*^[12] explored a mixed-halide argyrodites with the formula $\text{Li}_{6-x}\text{PS}_{5-x}\text{ClBr}_x$. The results showed that Cl^- , Br^- and S^{2-} co-occupied the 4a/4c sites. A maximum ionic conductivity of $2.4 \times 10^{-2} \text{ S cm}^{-1}$ in a sintered state could be observed in the $\text{Li}_{5.3}\text{PS}_{4.3}\text{ClBr}_{0.7}$ electrolyte, which is so far the highest value in the argyrodite family. The $\text{Li}_{5.3}\text{PS}_{4.3}\text{ClBr}_{0.7}$ electrolyte also possessed an extremely low activation energy of 0.155 eV, providing a promising possibility for its application under low-temperature conditions^[12]. In addition, introducing structural disorder in the crystalline $\text{Li}_6\text{PS}_5\text{I}$ electrolyte by a soft mechanical treatment can also enhance its ionic conductivity^[100].

STABILITY OF SULFIDE ELECTROLYTES

Electrochemical stability window

In addition to ionic conductivity, the electrochemical stability window of sulfide electrolytes is a crucial factor that affects the overall performance of sulfide-based ASSLBs. The decomposition of sulfide electrolytes results in high interfacial resistance and reduces the capacity of the batteries. Initially, the electrochemical stability window of sulfides was measured by cyclic voltammetry. Early experiments demonstrated that most sulfide electrolytes possess a remarkable electrochemical stability window up to 5 V vs. Li metal^[27,75,101,102]. For instance, the electrochemical window of $\text{Li}_6\text{PS}_5\text{X}$ (X = Cl, Br or I) argyrodites was characterized by Boulineau *et al.*^[27] with a Li/BM-Li₆PS₅X/stainless steel cell. There was a total absence of any electrochemical response, which illustrated that the $\text{Li}_6\text{PS}_5\text{X}$ (X = Cl, Br or I) electrolytes could remain stable at a voltage of 0.5–7 V vs. Li metal^[27]. Moreover, by applying a similar testing method, the iodide-based $\text{Li}_7\text{P}_2\text{S}_8\text{I}$ electrolyte and the oxygen-substituted $\text{Li}_{10}\text{GeP}_2\text{S}_{11.4}\text{O}_{0.6}$ electrolyte were discovered to display a stable electrochemical window up to 10 V vs. Li metal^[101,102].

In contrast, recent studies have suggested that the electrochemical windows of sulfide electrolytes were overestimated because the poor contact between the inert metal and solid electrolyte limits the reaction kinetics and hinders the mobility of Li⁺^[103,104]. DFT calculations were applied by Mo *et al.*^[101] and Bai *et al.*^[102] to predict the electrochemical windows of typical sulfides. It was found that sulfides display much narrower electrochemical windows than previously suggested experimentally, as displayed in Figure 10^[105,106]. A new Li/electrolyte/electrolyte-carbon cell configuration was proposed by Han *et al.*^[103] to correct the discrepancy between the theoretical calculations and experimental measurements. Mixing an electrolyte and carbon could increase the overall electronic conductivity of electrodes, which was beneficial for amplifying the decomposition current signal and reflecting the intrinsic electrochemical windows of sulfide electrolytes. Based on cycling voltammetry of the Li/LGPS/LGPS-C/Pt cell, it was found that the LGPS electrolyte would be reduced at 1.7 V and oxidized at 2.1 V, consistent with the theoretical calculation results^[103].

Chemical stability in humid air

The chemical stability against humid air is another concern regarding the application of sulfide electrolytes. Most sulfide electrolytes suffer from poor moisture stability and generate toxic H₂S gas upon contact with humid air. Therefore, the common preparation process of sulfide electrolytes is usually under the protection of inert gas (argon). Numerous surveys of the moisture stability of sulfide electrolytes have been carried out. For example, the air stability of the Li_xPS₅Cl electrolyte was characterized with XRD measurements. Several clear impurity peaks could be observed after exposing the Li_xPS₅Cl electrolyte to humid air for 10 min and its ionic conductivity deteriorated from 1.8×10^{-3} S to 1.56×10^{-3} , 1.43×10^{-3} and 8.7×10^{-4} S cm⁻¹ after exposure to air for 10 min, 1 h and 24 h, respectively^[107]. The chemical stability of sulfide electrolytes in the Li₂S-P₂S₅ system was also investigated by Muramatsu *et al.*^[108] in humid atmosphere. There was no obvious structure change in the PS₄³⁻ ions after exposure to air, while the S²⁻ and P₂S₇⁴⁻ ions displayed a clear structural change and significant amounts of toxic H₂S gases were generated. As a consequence, a conclusion was drawn that PS₄³⁻ ions possess higher chemical stability compared to other phosphate ions^[108].

The hard-soft-acid-base theory has been proposed by Liang *et al.*^[49] to explain the poor chemical stability of sulfide electrolytes and has been applied to inhibit their deterioration. In P-containing sulfide electrolytes, the hard acid (P) tends to bond with the hard base (O) in humid air to form P-O bonds rather than maintaining the pristine P-S bonds. Furthermore, S atoms tend to bond with the H atoms in humid air, resulting in the generation of H₂S. Therefore, replacing the soft base (S) with a hard base (O) or replacing the hard acid (P) with a soft acid is a feasible approach to improve the air stability of sulfide electrolytes according to the hard-soft-acid-base theory. Based on this, many successful experiments for improving the air stability of sulfides have been reported^[48,49,109]. In the Li₂S-P₂S₅ glass electrolytes, substituting partial P₂S₅ with P₂O₅ could effectively reduce the release rate of H₂S gas, illustrating that the air stability of electrolytes was improved with O substitution^[109]. In addition, replacing hard acid (P) with soft acid (Sb, Sn and so on) was a good choice to enhance the air stability^[48,49]. Liang *et al.*^[49] investigated the effect of Sb substitution in Li₁₀Ge(P_{1-x}Sb_x)₂S₁₂ electrolytes. As depicted in Figure 11A and B, Sb prefers to substitute P at the 4d site. It was discovered that there was no appearance of additional or broadening peaks after exposing the Sb-substituted electrolytes to humid air for 24 h. In addition, theoretical calculations and experimental tests demonstrated that Sn-substituted Li_xPS₅I electrolytes possessed better air stability than the pristine Li_xPS₅I electrolyte because of the stronger Sn-S bonds^[48].

SULFIDE ELECTROLYTE/LI METAL ANODE INTERFACE

Challenges for the sulfide electrolyte/Li metal anode interface

Interfacial side reactions and Li dendrites are two concerns that have plagued the development of liquid-state lithium-metal batteries for a long time^[110]. These issues also exist when applying lithium metal as the anode in an ASSLBs^[111,112]. Similar to typical sulfide electrolytes, high-valent cations in anion clusters, such

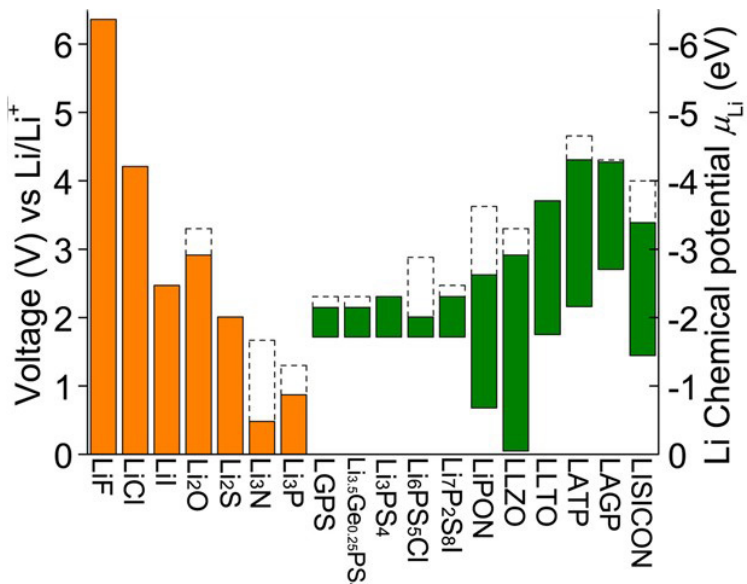


Figure 10. Calculated electrochemical stability windows for a variety of solid electrolytes. The dashed lines mark the oxidation potentials to fully delithiate the material. Reproduced with permission^[106] (Copyright 2015, American Chemical Society).

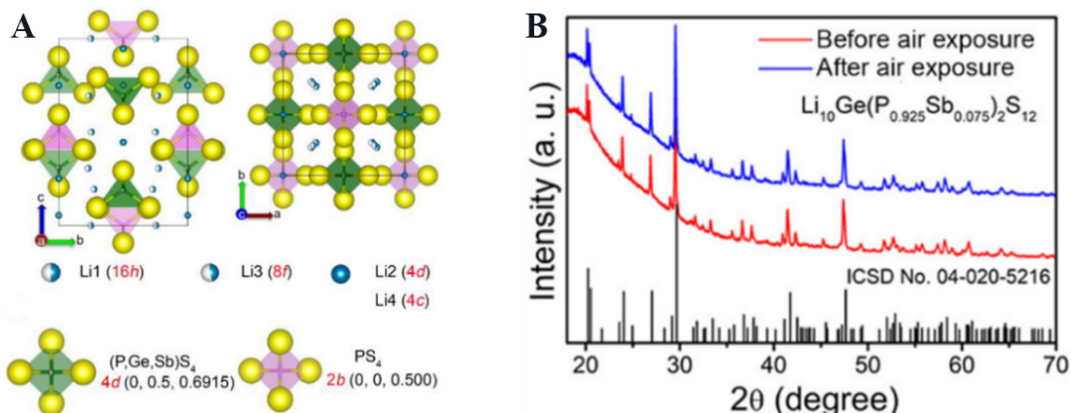


Figure 11. (A) Crystal structure of $\text{Li}_{10}\text{Ge}(\text{P}_{0.925}\text{Sb}_{0.075})_2\text{S}_{12}$. (B) XRD patterns of $\text{Li}_{10}\text{Ge}(\text{P}_{0.925}\text{Sb}_{0.075})_2\text{S}_{12}$ sample before and after air exposure. Reproduced with permission^[49] (Copyright 2020, American Chemical Society). XRD: X-ray diffraction.

as P^{5+} , Ge^{4+} , Sn^{4+} and so on, can easily react with Li metal [Figure 12B], resulting in an enhancement in Ohmic resistance and a decrease in Coulombic efficiency (CE)^[113]. Theoretically, dendrite growth should be prohibited in solid electrolytes for the reason that the bulk modulus of solid electrolytes is higher than that of Li metal. However, the issue of dendrites tends to be severer in ASSLBs^[114,115]. The theory of dendrite growth in solid electrolytes is diverse and is introduced in detail below. Unlike liquid electrolytes, which can directly wet the electrodes, the solid/solid contact in ASSLBs is not satisfactory. Although sulfide electrolytes display a better contact than oxide electrolytes, the contact loss at the sulfide electrolyte/anode interface during Li stripping/plating enlarges the local current density and leads to rapid dendrite growth^[116].

Interfacial reactions

Li metal has the lowest reduction potential (-3.04 V vs. SHE), which means it has excellent potential in the application of energy storage systems. However, the low reduction potential of Li metal also indicates that

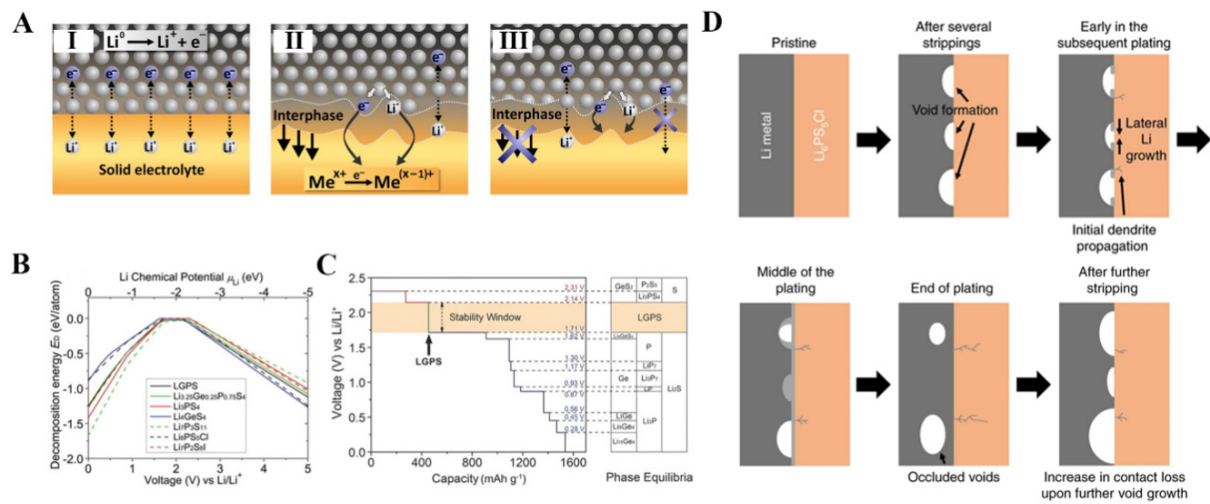


Figure 12. (A) Types of interfaces between lithium metal and a solid lithium ion conductor: (I) a non-reactive and thermodynamically stable interface; (II) a reactive and mixed conducting interphase; (III) a reactive and metastable solid-electrolyte interphase (SEI). Reproduced with permission^[117] (Copyright 2015, Elsevier). (B) Decomposition energy E_D of sulfide electrolyte as a function of applied voltage Li. Reproduced with permission^[106] (Copyright 2015, American Chemical Society). (C) First-principles calculation results of the voltage profile and phase equilibria of LGPS during lithiation and delithiation. Reproduced with permission^[103] (Copyright 2016, Wiley-VCH). (D) Schematic of Li metal/Li₆PS₅Cl interface cycled at an overall current density above the CCS. Reproduced with permission^[116] (Copyright 2019, Springer Nature Publishing AG).

the interfacial reactions between an electrolyte and Li metal are almost inevitable. Typically, in organic electrolyte research, Li metal is oxidized by solvents or Li salts to form an SEI, which can protect Li metal from further corrosion. In solid electrolytes, the property of the interphase is more complex.

Three types of Li/solid-state electrolyte interphase have been identified according to the mainstream theory [Figure 12A]^[117]. Type I includes all the thermodynamically stable solid electrolytes against Li metal. In this case, no interfacial reactions occur. For instance, several researchers have reported that LIPON and Li are in thermodynamic equilibrium. Unfortunately, sulfide electrolytes are included this type because their anionic clusters are easily reduced by Li metal.

The type II interphase is unique and arises from the reaction between Li and solid electrolytes containing metal ions. The reaction products consisting of electronic conductors (Li alloys) and ionic conductors continue to react with electrolytes. The so-called mixed conducting interphase is common in sulfide electrolytes. During the cycling of Li || LGPS || Li symmetric cells, the voltage polarization keeps rising due to continuous side reactions. By analyzing the X-ray photoelectron spectroscopy (XPS) spectra of the Li || LGPS interphase, Li-Ge alloys, which are the reaction products from Li and GeS₄⁴⁻ should be the origin of the unstable interphase^[118]. Furthermore, a theoretical study has predicted the reaction products of Li and GeS₄⁴⁻ [Figure 12C].

For type III, the interphase reaction still occurs between Li and solid electrolytes but the reaction products that are thermodynamically stable against Li could prevent the reaction from proceeding. This type of interphase plays a similar role as the SEI. For example, Li₆PS₅Cl and Li react to form Li₂S, Li₃P and LiCl^[60,116]. The resistance of Li-Li symmetric cells incorporated with Li₆PS₅Cl does not continue to increase because the reaction products of Li and Li₆PS₅Cl are rather stable against Li. The side reactions between Li and electrolytes lead to a drop in CE and present a bottleneck in the development of high-energy-density Li-metal batteries (LMBs). In particular, for sulfide electrolytes containing relatively unstable anionic clusters,

the interphase of type II should be avoided and the influence of type III should be limited to a certain level.

Li dendrites

Li dendrites are central factors that hinder the commercial application of LMBs. These needle-like crystals pierce the membrane and cause short-circuit to the whole-cell effortlessly^[119]. Thermodynamically, the growth regimes of dendrites are linked with the intrinsic energetic properties of metal surfaces^[120]. Therefore, the epitaxial and mossy growth of bare Li during the electrochemical process is inevitable.

Ideal solid electrolytes with high ionic conductivity and no electronic conductivity are proposed to take the place of traditional membranes and liquid electrolytes in LMBs. Compared to soft and porous membranes, ideal solid electrolytes possess high bulk moduli and are obviously denser after applying pressure^[121]. Moreover, it is well known that the organic electrolytes utilized in liquid-state LMBs are combustible, yet the ignition points of solid electrolytes are much higher. Although, this initially inspired significant research into the commercialization of ASSLBs, the dendrite problem is not solved by solid electrolytes^[115,122]. Recently, the growth of Li dendrites in solid electrolytes was clearly displayed by a high-resolution *in-situ* optical microscope, implying that solid electrolytes still had the conditions for dendrite growth^[122]. By experimental observation, the voids in solid electrolytes provide a suitable environment for Li dendrites to grow. Furthermore, it has been reported that the grain boundaries of solid electrolyte may support dendrite growth due to their different nature from the bulk crystal^[115,123,124]. Recently, Han *et al.*^[125] tested the electronic conductivity of typical oxide, LIPON, and sulfide electrolytes and found that the role of electronic conductivity in dendrite growth could not be ignored. Neutron depth profiling was also applied to visualize dendrite growth. By correlating the critical current densities with electronic conductivity, they proposed a criterion where the electronic conductivity of the solid electrolyte should be considered when designing practical solid electrolytes.

Contact loss at the sulfide/anode interface

Solid-solid contact remains a key issue in ASSLBs. Sulfide electrolytes, due to their soft characteristics, possess good interphase compatibility with Li metal. The pellets of sulfide electrolytes can be directly assembled into cells without any treatment. However, during the process of Li stripping/plating, the interphase initially in close contact becomes loose. The explanation for this phenomenon can be briefly concluded by the rate of Li creeping. Pits and holes form when Li is stripped from the bulk. These pits and holes can be filled to some extent by the creeping of Li metal, but the reality is that the rate of Li creeping is far lower than the rate of Li stripping. Thereafter, the next Li plating process is affected by the existence of pits and holes, resulting in insufficient contact between the Li and sulfide electrolytes. Therefore, when the external current density is constant, the contact loss between sulfide electrolytes and Li metal leads to an exponential rise in local current density at the contact point of the sulfide and Li metal.

According to Sand's theory, the rate of dendrite growth is positively related to current density^[126]. It is not arduous to draw the conclusion that the contact loss of sulfide/Li interphase plays a major role in the failure of ASSLBs. Kasemchainan *et al.*^[116] carried out detailed research on the relationship between the morphology of the interphase and cell performance. Via characterization of cross-sectional SEM and *in situ* X-ray computed tomography, voids were shown to form after several stripping cycles. Though the process of Li plating could decrease the number of voids, some occluded voids still existed when the current density was above the critical stripping current. After further stripping, the voids grow and the contact loss at the Li/sulfide interphase is severer. Once the local current density is above the threshold for dendrite formation, short circuit and cell failure occur as a result [Figure 12D]. The contact loss of the sulfide/Li interphase may be the reason that dendrite problems have still not been solved in sulfide-based ASSLBs.

Strategies to stabilize the sulfide electrolyte/Li metal anode interface

Benefiting from our successful experience and methods in liquid-state Li-metal batteries and sodium-ion batteries^[127-129], improving the interphase compatibility between sulfides and Li metal is achievable^[130,131]. So far, the strategies to stabilize the sulfide/Li metal interphase can be considered as tuning the composition of sulfide electrolytes or anodes and constructing an artificial SEI or interlayer^[2,132]. Although none of these methods thoroughly solve the dilemma of interphase incompatibility, the theory and experience generated during the process of inquiry are certainly worthwhile. A summary of the performance of Li-Li symmetric cells using sulfide electrolytes is given in [Table 3](#).

Composition tuning of sulfide electrolytes

According to Sand's theory, the origin of dendrite growth starts from uneven Li deposition^[126]. In ASSLBs, promoting the rate of Li diffusion could release the Ohmic polarization. On this basis, a more homogenous Li deposition can be realized. Considering that interfacial side reactions are closely related to the properties of sulfide electrolytes, the targets for the composition tuning of sulfides should not only focus on enhancing the ionic conductivity. Indeed, improving the diffusion rate of Li^+ could somehow promote a more homogenous Li^+ flux during Li plating/stripping, but sulfide electrolytes doped with high-valent metal ions can form an unstable mixed conductive interphase. Hence, maintaining high ionic conductivity while decreasing the overall side reactions represents a conventional route for modifying the composition of sulfide electrolytes to obtain better anodic stability^[145].

The investigation of Li/sulfide interphases by XPS and the calculation of the grand potential phase diagram have proved that sulfur anion clusters centered on high-valent cations (e.g., PS_4^{3-} , BS_4^{5-} , SiS_4^{4-} , GeS_4^{4-} and so on) are responsible for side reactions^[146]. For non-metal high-valent cations with less reduction activity, replacing partial S atoms with O atoms could decrease the side reactions. A theoretical phase diagram study proposed that Li_3PO_4 is metastable against Li metal^[147]. Thus, Tao *et al.*^[30] added certain amounts of P_2O_5 into $75\text{Li}_2\text{S}-25\text{P}_2\text{S}_5$ glass-ceramic electrolytes to improve the ionic conductivity and anodic stability. It was discovered that the glass-ceramic electrolytes substituted with 1 mol% P_2O_5 had good electrochemical performance. The $\text{Li}||\text{Li}$ symmetric cells incorporated with modified electrolytes displayed a lower polarization and longer cycling life than the cells using $75\text{Li}_2\text{S}-25\text{P}_2\text{S}_5$ glass-ceramic electrolytes at a current density of 0.1 mA cm^{-2} and a cutoff capacity of 0.1 mAh cm^{-2} , indicating that both the side reactions and dendrite growth were suppressed. Ideally, the side reactions between sulfide electrolytes and Li metal should be eliminated. However, with the existence of sulfur anion clusters centered on high-valent cations, prohibiting the decomposition of sulfide electrolyte in anodic sides by tuning its composition is almost impossible. Thus, it is worthy of consideration to select a proper doping component that can generate a robust passivation layer on the surface of Li metal.

LiX ($\text{X} = \text{F}, \text{Cl}, \text{Br}$ or I) is widely used as a dopant in sulfide electrolytes due to its mechanical and electronical properties^[90]. Han *et al.*^[135] introduced different amounts of LiI into a $75\text{Li}_2\text{S}-25\text{P}_2\text{S}_5$ glassy system to regulate its reactivity and ionic conductivity. The glass electrolyte with a composition of $0.7(\text{Li}_2\text{S-P}_2\text{S}_5)-0.3\text{LiI}$ possessed high ionic conductivity and a critical current density (CCD) above 1 mA cm^{-2} . The promoted anodic stability was attributed to the introduction of LiI into the Li/electrolyte interphase. LiI could help to lower the electronic conductivity of the interphase based on a larger bandgap of LiI (6.4 eV) compared to that of Li_3P (0.7 eV). Furthermore, incorporating LiI into interphase increase the ionic conductivity of the interphase so that the mobility of Li atoms could be improved.

LiF is an essential component in traditional LIBs to stabilize the interphase. By DFT calculations, it was reported that LiF possesses a strong ability to suppress dendrite growth. Though the ionic conductivity of bulk LiF is relatively low, researchers have found that nano-LiF distributed in the interphase displayed a

Table 3. Summary of the performance of Li-Li symmetric cells using sulfide electrolytes

No.	Cell configuration	Critical current density (mA cm ⁻²)	Cut-off capacity (mAh cm ⁻²)	Test temperature	Ref.
1	Li/Li _{6.3} P _{0.9} Cu _{0.1} S _{4.9} Cl _{1.1} /Li	3.0	3.0	50 °C	[133]
2	Li/Li _{6.25} PS _{4.75} ClN _{0.25} /Li	1.52	1.52	RT	[60]
3	Li/Li ₆ PS ₅ Cl _{0.3} F _{0.7} /Li	6.37	5.0	RT	[134]
4	Li/0.7(Li ₂ S-P ₂ S ₅)-0.3Li/Li	3.9	3.9	100 °C	[135]
5	Li/G-LGPS-G/Li (50 MPa)	10.0	0.25	RT	[136]
6	Li/Li ₇ P _{2.88} Nb _{0.12} S _{10.7} O _{0.3} /Li	1.16	1.16	RT	[8]
7	Li/Li ₃ N-LiF//Li ₃ PS ₄ //Li ₃ N-LiF/Li	6.0	6.0	RT	[137]
8	Li/LiMg22/LGPS/LiMg22/Li	1.3	1.3	RT	[138]
9	Li/LiFSI@Li ₃ PS ₄ /Li	2.0	2.0	RT	[121]
10	Li-Bp-DME/Polyoxyethylene (PEO)/Li ₃ PS ₄ /PEO/Li-Bp-DME	17.78	17.78	30 °C	[139]
11	Li/Graphite-Li ₆ PS ₅ Cl-LGPS-Li ₆ PS ₅ Cl-Graphite Li	20.0	0.25	55 °C	[140]
12	Li/Li ₂ P ₃ S ₁₁ /Li	0.76	0.76	RT	[141]
13	Li/0.75Li ₂ S-0.25P ₂ S ₅ /Li	0.4	0.4	RT	[135]
14	Li/0.6Li ₂ S + 0.32SiS ₂ + 0.12PS _{5/2} /Li	1.50	1.50	RT	[142]
15	Li/Li ₆ PS _{4.7} O _{0.3} Br/Li	0.90	0.90	RT	[143]
16	Li/Li ₆ PS ₅ Cl/Li	0.55	0.55	RT	[144]
17	Li/Li ₇ P _{2.9} S _{10.05} S _{10.85} /Li	0.80	0.80	RT	[141]

RT: Room temperature.

satisfactory ionic conductivity^[148]. Recently, Zhao *et al.*^[134] reported a F-containing sulfide electrolyte to derive the formation of a functional SEI layer with a high concentration of LiF. Li₆PS₅Cl was selected as a host material to realize F doping in their work. The Li symmetric cells incorporated with an optimized electrolyte Li₆PS₅Cl_{0.3}F_{0.7} delivered a stable cycle performance at an ultrahigh current density of 6.37 mA cm⁻² and a cut-off capacity of 5 mA cm⁻². A detailed investigation of interphase by XPS depth profiling and time of flight-secondary ion mass spectrometry proved the existence of LiF throughout the interphase. Compared to unmodified Li₆PS₅Cl, the F-containing electrolytes effectively passivate the interphase and suppress dendrite growth.

Moreover, accompanied by the success of Li₃N-rich SEI in LMBs using organic electrolytes, Liu *et al.*^[60] substituted partial Cl atoms in Li₆PS₅Cl with N atoms. On this basis, an *in-situ* formed Li₃N-rich interphase was introduced. By galvanostatic cycling Li symmetric cells at step-increased current densities, the electrolyte with a composition of Li_{6.25}PS_{4.75}ClN_{0.25} displayed a CCD over 1.5 mA cm⁻². Based on DFT calculations, N atoms near the Li/electrolyte interphase are not easily pulled into the lattice of metallic Li to form Li-N bonds [Figure 13A and B]. In addition, incorporating Li₃N into the interphase can fasten the transport of Li⁺. On this basis, homogenous Li plating was realized.

Very recently, an unconventional work has brought inspiration to the composition tuning of sulfides. Although it is true that metal cations in sulfides can easily react with Li metal, when the doped metal cations are not the dominant components, the disadvantages can be compensated for. Taklu *et al.*^[133] reported a sulfide super-conductor Li_{6.3}P_{0.9}Cu_{0.1}S_{4.9}Cl_{1.1} with high stability against Li. Despite the existence of Cu⁺, the Li_{6.3}P_{0.9}Cu_{0.1}S_{4.9}Cl_{1.1} electrolyte with much lower electronic conductivity and better interphase compatibility than typical Li₆PS₅Cl. Thus, the dendrite growth would be prohibited. The released interphase incompatibility and low electronic conductivity compensated for the effects of side reactions. Consequently, the CCD of Li_{6.3}P_{0.9}Cu_{0.1}S_{4.9}Cl_{1.1} can reach 3 mA cm⁻² at 50 °C, which is four times higher than that of typical

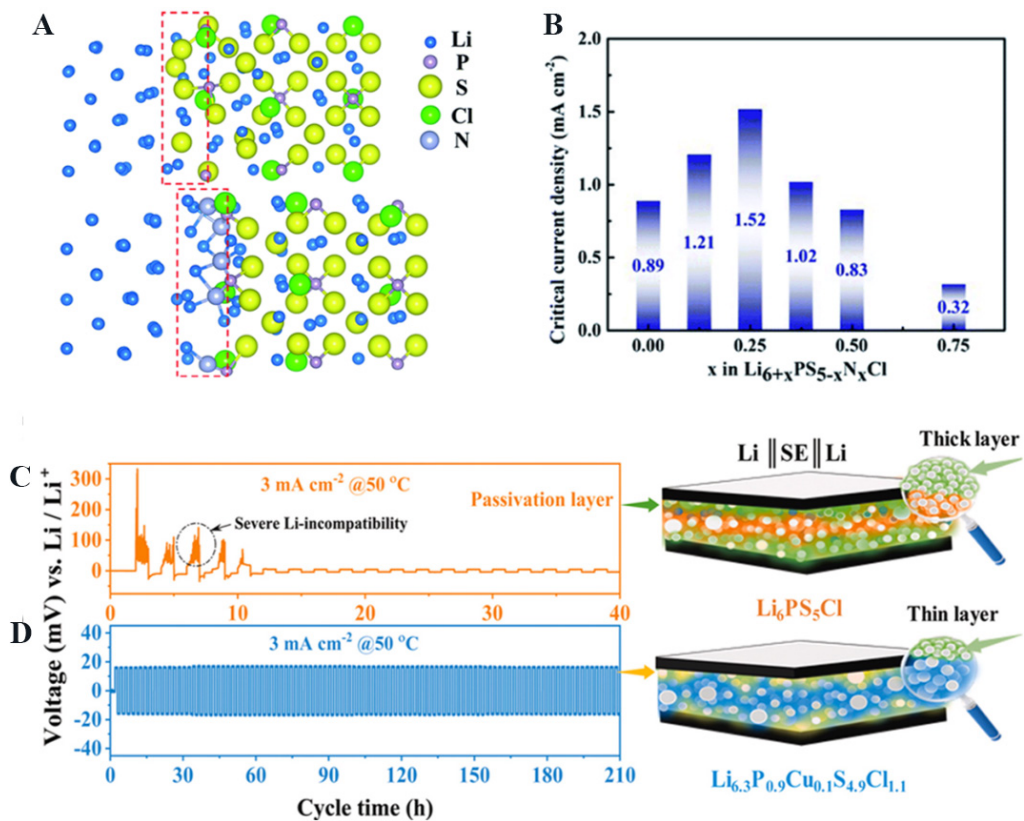


Figure 13. (A) Interface configuration for Li/Li₆PS₅Cl (top) and Li/N-doped Li₆PS₅Cl (below) after structure relaxation by DFT calculations. (B) Critical current densities of Li_{6+x}PS_{5-x}N_xCl electrolytes as a function of N content x. Reproduced with permission^[60] (Copyright 2021, Royal Society of Chemistry). Galvanostatic symmetric cell, Li | SE | Li voltage profiles at 50 °C. (C) and (D) Li plating and stripping performance of Li₆PS₅Cl and Li_{6.3}P_{0.9}Cu_{0.1}S_{4.9}Cl_{1.1} at 3 mA cm⁻², respectively. Reproduced with permission^[133] (Copyright 2021, Elsevier).

Li₆PS₅Cl. In addition, when cycling the symmetric cells at a current density of 3 mA cm⁻², the performance of Li_{6.3}P_{0.9}Cu_{0.1}S_{4.9}Cl_{1.1} is much better than that of Li₆PS₅Cl [Figure 13C and D].

Composition tuning of anodes

It is clear that employing pure Li metal as an anode acquires high energy density, but it is also acceptable to sacrifice part of the energy density in exchange for stability. Through DFT calculations and experimental observations, Li alloys have relatively high reduction potentials compared to Li metal^[149]. Therefore, the side reactions between the anode and sulfide electrolyte will not proceed violently. Furthermore, it is also proved that the diffusion rate of Li⁺ on some Li alloys is higher than that on Li metal^[150]. A fast diffusion rate of Li⁺ on anodes could decrease the growth of dendrites. Li-In alloys, for instance, are widely used as anodes in assembling ASSLBs^[151]. The reduction potential of Li-In alloys is ~0.6 V above Li metal. For this reason, the side reactions between anodes and electrolytes are prohibited^[152]. Moreover, the soft nature of Li metal does not change significantly in Li-In alloys, which ensures good contact between the Li and electrolytes^[153]. However, it is not practical to use Li-In alloys for commercialization given that In is not affordable for large-scale generation. Furthermore, the high density of In and high reduction potential of Li-In alloys decrease the overall energy density of ASSLBs. Therefore, only experimental work investigating cathodic or anodic unstable electrolytes would apply Li-In as anodes.

Lee *et al.*^[154] demonstrated a silver/carbon composite anode that could mitigate the problems of low CE and dendrite growth in ASSLBs at high current densities. It was proved by cross-sectional SEM and corresponding energy dispersive spectroscopy that nano-Ag particles can be alloyed with Li during the process of Li plating. In addition, partial Ag was found to move to the current collector side, which assisted the uniform and dendrite-free plating of Li metal. The Ag-C/LiNi_{0.8}Co_{0.1}Mn_{0.1}O₂ (NCM811) pouch cells exhibited high energy density ($> 900 \text{ Wh L}^{-1}$) and stable cycling for over 1000 times. Recently, Tan *et al.*^[155] developed a micro-silicon anode to realize high-energy-density ASSLBs. During the lithiation process of micro-silicon, the formation of Li-Si alloys can propagate throughout the anode, benefiting from the good ionic and electronic contact between Li-Si and micro-silicon particles. The assembled micro-silicon/NMC811 full cell could deliver a capacity retention of ~80% after 500 cycles at a current density of 5 mA cm⁻², demonstrating the robustness of the constructed micro-silicon anodes. Choi *et al.*^[156] proposed Ag-Li alloy anode via a mass-producible roll-pressing method [Figure 14A]. The *in-situ* formed Ag-Li intermetallic layer mitigated uneven Li plating, as confirmed by the improved cycling performance of Ag-Li/Ag-Li symmetric cells [Figure 14B]. ASSLBs with Ag-Li anodes displayed a capacity retention of 94.3% for 140 cycles, while the cells with unmodified Li metal showed frequent initial short-circuit. In addition, Su *et al.*^[136] applied a Li/graphite composite as the anode, where the graphite served as a protective layer to suppress the side reactions between Li and LGPS. Under a pressure of 250 MPa, the symmetric cells with Li-graphite composite anodes could cycle at a current density of 10 mA cm⁻² with no occurrence of short circuit or dendrite growth.

In addition to the construction of Li alloy anodes, Peng *et al.*^[139] prepared a liquid lithium solution anode by putting Li metal into a biphenyl/DME solution at 60 °C. It has been reported that the contact loss between a sulfide and Li metal causes dendrite problems. The introduction of the liquid lithium solution anode continuously ensured the contact between anode and electrolytes, thus prohibiting dendrite growth. As a result, the symmetric cells incorporated with liquid lithium solution anodes, a Li₃PS₄ pellet and polyoxyethylene (PEO) protective layers [Figure 14C] achieved a record-high CCD of $> 17.78 \text{ mA cm}^{-2}$ [Figure 14D]. The repeatability and strictness of the CCD measurement was proved by adding stable cycling for three times at some particular current densities into the step-increase test of CCD for a Li-Bp-DME/PEO/LPS/PEO/Li-Bp-DME cell [Figure 14E]. An ultrahigh current density of 10.16 mA cm⁻² was achieved with a per-cycle plating areal capacity of 3.81 mAh cm⁻², thereby confirming that the cell has a superior lithium dendrite suppression ability.

Construction of artificial SEIs

Artificial SEIs have proved to be effective in suppressing side reactions and dendrite growth in liquid-state LMBs. The experience obtained from the design of appropriate artificial SEIs in previous research on liquid-state LMBs also aids the design of artificial SEIs in ASSLBs. The success of high concentration electrolytes in liquid-state LMBs is attributed to anion-derived SEIs^[157]. Based on this, Fan *et al.*^[121] processed Li with 6 M LiFSI in DME to form a LiF-rich interphase between Li and a sulfide electrolyte. After drying the organic electrolytes, galvanostatic charging/discharging tests on symmetric cells using Li₃PS₄ as an interlayer were performed. The symmetric cells incorporated with the LiF-rich interphase displayed a CCD value of $> 2 \text{ mA cm}^{-2}$, indicating that this interphase effectively prohibited the growth of dendrites. Zhang *et al.*^[158] proposed a surface phosphating method of Li metal to suppress the side reactions between Li and LGPS. Symmetric cells with a LiH₂PO₄-rich interphase could maintain stability at 0.1 mA cm⁻² for over 950 h without obvious polarization. Furthermore, Liang *et al.*^[159] constructed a SEI consisting of amorphous Li_xSiS_y by two steps of liquid phase reactions on Li metal [Figure 15A]. Through thermogravimetric analysis of the anodes, the modified anodes were verified to be air stable. The amorphous Li_xSiS_y coated on Li metal enabled fast Li diffusion, thereby preventing the formation of voids and cracks. As a result, symmetric cells with Li_xSiS_y-coated Li could stably cycle at a current density of 0.1 mA cm⁻² and 0.5 mAh cm⁻² for over

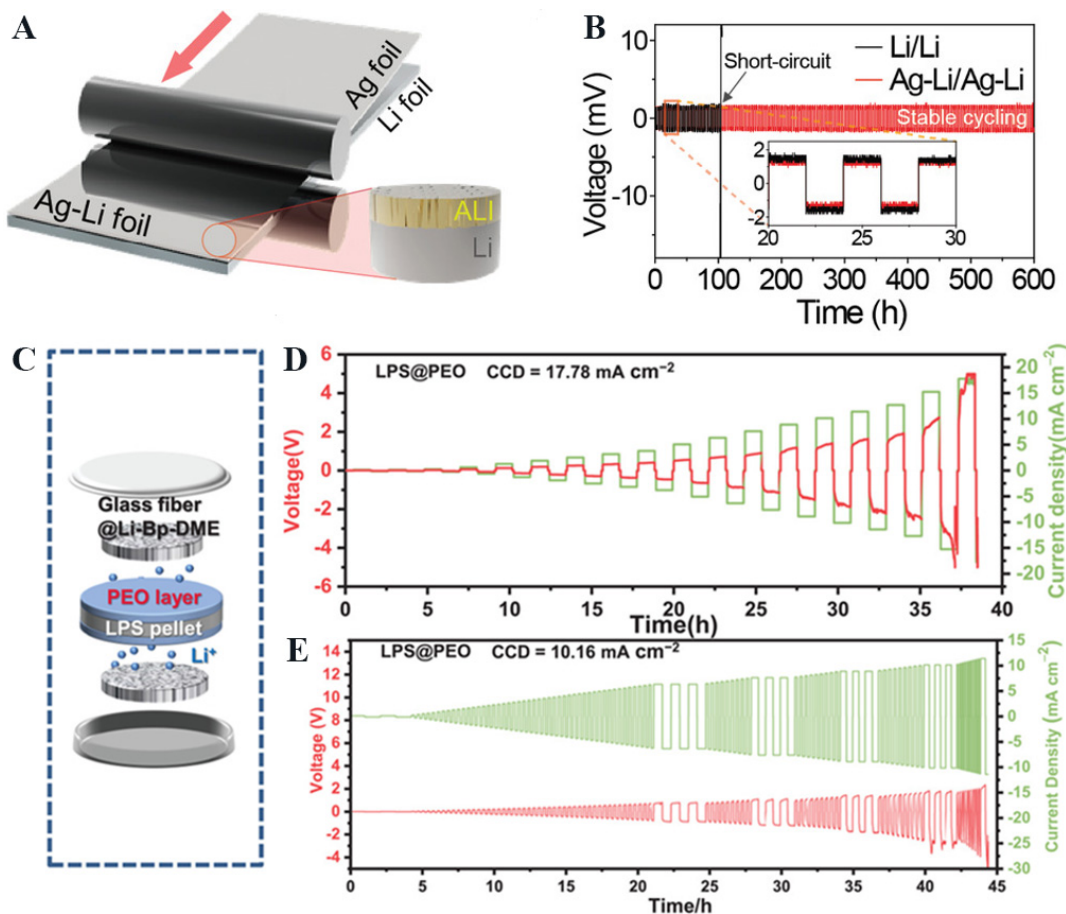


Figure 14. (A) Experimental scheme for preparing Ag-Li alloy foil. (B) Voltage profiles of Li/Li and Ag-Li/Ag-Li symmetric cells at 0.5 mA cm^{-2} with a fixed capacity of 1 mAh cm^{-2} . Reproduced with permission^[156] (Copyright 2021, Wiley-VCH). (C) Schematic illustration of the symmetric coin cell used for CCD detection. (D) Voltage profiles of the symmetric cell using PEO protective layer at step-increased current densities and the cell cycled once under each current density. (E) Voltage profiles of the symmetric cell using PEO protective layer at increased current densities and the cell cycled three times under some particular current densities. Reproduced with permission^[139] (Copyright 2021, Wiley-VCH). CCD: Critical current density; PEO: polyoxyethylene.

2000 h [Figure 15B], while the symmetric cells with bare Li could only cycle at the same conditions for less than 20 h.

Recently, based on a theoretical study of the mechanical and chemical properties of typical SEI components. Ji *et al.*^[137] designed a Li₃N-LiF hybrid coating on Li₃PS₄ to assure a high ionic conductivity and interphase energy. As a consequence, a record-high CCD value of $> 6 \text{ mA cm}^{-2}$ was achieved. Furthermore, according to the experimental results and DFT calculations, the criteria for designing SEIs in ASSLBs were proposed in their work. Firstly, a good SEI should be electrochemically stable to metal Li to avoid additional side reactions. It should also have high ionic conductivity to enable the homogenous and fast diffusion of Li⁺ and have low electronic conductivity to block the transport of electrons through the interphase. The high interphase energy of SEI could help to suppress dendrite growth. These criteria cannot only guide the design of artificial SEIs but could also provide a standard to evaluate the interphases between Li and solid electrolytes.

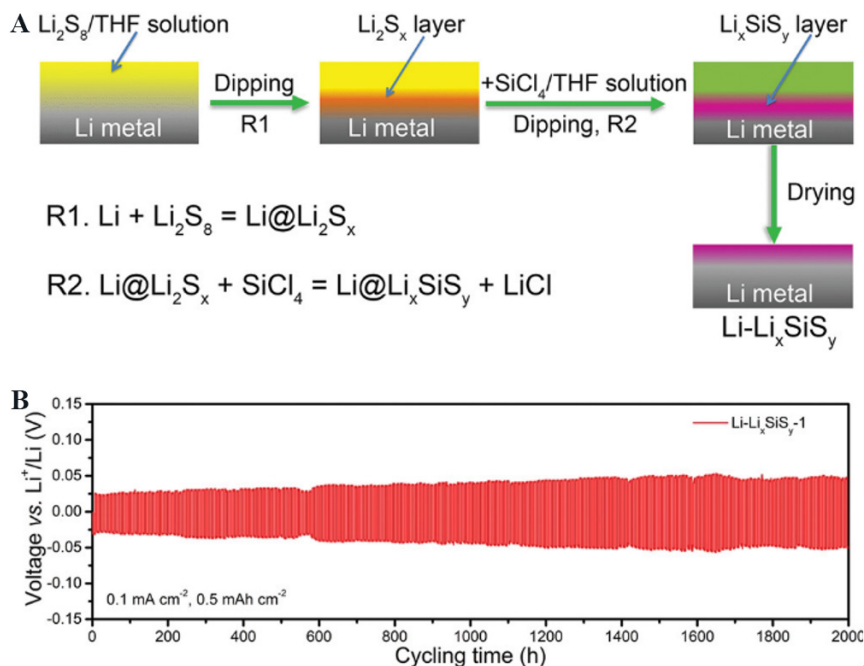


Figure 15. (A) Reaction scheme for the formation of $\text{Li-Li}_x\text{SiS}_y$ and the characterization of the $\text{Li-Li}_x\text{SiS}_y\text{-}1$ electrode. (B) Long-term cycling performance of symmetric $\text{Li-Li}_x\text{SiS}_y$ cells. Reproduced with permission^[159] (Copyright 2019, Wiley-VCH).

It is noteworthy that most previous work on the construction of artificial SEIs did not consider contact loss. Yang *et al.*^[160] performed large-scale molecular dynamics simulations to investigate the interphases between Li and solid electrolytes. The interphase failure started with the formation of nanosized pores by their observations. By correlating the interphase behavior and interfacial adhesion energy, it was discovered that the interphases between Li and solid electrolytes with higher interfacial adhesion energy displayed a better ability to avoid contact loss. Incoherent Li-solid electrolyte interphases with high interfacial adhesion energy require less applied external pressure. Therefore, future research into interphases should focus more on adhesion energy since the contact loss plays a significant part in dendrite growth.

Construction of interlayers

The construction of interlayers is a new perspective in ASSLBs. Firstly, it was found that ASSLBs incorporated with bilayer inorganic composite electrolytes displayed good cycling behavior during discharging and charging. In particular, for the electrolytes that have unsatisfactory anodic or cathodic stability, constructing another protective interlayer is effective. Based on DFT calculations, sulfide electrolytes containing iodine suffer from low cathodic stability. It is well known that sulfide electrolytes containing high-valent metal ions can easily react with Li metal. Therefore, Zhao *et al.*^[48] applied bilayer inorganic composite electrolytes when assembling ASSLBs. The Li-S ASSLBs with bilayer inorganic electrolytes could obtain a capacity retention of 96% after 200 cycles. Recently, Ye *et al.*^[140] designed a structure of a less stable LGPS electrolyte sandwiched between more stable electrolytes of $\text{Li}_6\text{PS}_5\text{Cl}$, which could prohibit dendrite growth through localized decomposition in the LGPS layer. To explain this, they proposed a mechanism analogous to the expansion screw effect, which is, any cracks in LGPS would be filled by dynamically generated decompositions. When utilizing graphite-covered Li as an anode, the symmetric cells could stably cycle over 1800 h at a current density of 0.25 mA cm^{-2} at RT. Moreover, this kind of symmetric cell could also cycle at an ultrahigh current density of 20 mA cm^{-2} . This effect could partially explain why well-designed bilayer inorganic composite electrolytes have good electrochemical performance.

Secondly, the building of polymer electrolyte layers between the Li and sulfide electrolytes is of great importance in solving the dilemma of contact loss during Li plating/stripping. Polymer electrolytes have a certain degree of fluidity, which can ensure the wetting of Li metal during cycling. Furthermore, altering the components of the polymer electrolytes provides a new strategy for constructing SEIs in ASSLBs. Inspired by the moderation and long duration of sustained release drug-carriers in the biomedicine, Chen *et al.*^[161] prepared LiTFSI/PPC polymer electrolytes. During cycling, PPC decomposes into PC to release LiTFSI, which reacts with Li metal [Figure 16A]. As a consequence, a LiF-rich interphase forms to suppress dendrite growth. As a result, symmetric cells containing polymer-coated Li displayed stable cycling and relatively low polarization at a current density of 0.5 mAh cm⁻² for over 300 h [Figure 16B and C].

Li *et al.*^[162] also synthesized a gel electrolyte originating from the polymerization of 1,3-dioxolan initiated by lithium difluoro(oxalato)borate. By adding certain amounts of LiPO₂F₂ as a SEI forming agent, a robust SEI containing Li₃PO₄ and LiF was obtained. The side reactions and dendrite growth were efficiently suppressed by the synthesized gel electrolytes. At a current density of 0.5 mA cm⁻² and a cut-off capacity of 0.5 mAh cm⁻², the symmetric cells with polymer/LGPS layers could cycle for 500 h without almost any polarization compared to the symmetric cells with only LGPS as the interlayer, which indicated that the severe side reactions between Li and LGPS were prohibited. Using backscattered electron imaging characterization, a clear black spot appeared in LGPS without the protection from polymer electrolytes, while there was no obvious change in the LGPS electrolytes protected by synthesized polymer electrolytes. The appearance of black spots means dendrite growth through the observed area because the electron conductivity of Li is much higher than the electrolyte.

SULFIDE ELECTROLYTE/CATHODE INTERFACES

Challenges for sulfide electrolyte/cathode interfaces

The challenges facing sulfide electrolyte/cathode interfaces originate from the sharp electrochemical window of sulfides and insufficient contact between cathode particles and sulfides. Firstly, based on the above-mentioned DFT calculation results, sulfide electrolytes are not able to sustain high-voltage environments. Therefore, oxidation compositions of sulfides occur during the process of charging. Moreover, contact loss between solid and solid particles during cycling and violent volume change of cathodes contribute significantly to the failure of ASSLBs. Finally, the formation of the space charge layer in the interphase between sulfides and cathode particles hinders the transport of charge carriers.

Space charge layers

The space charge layer is a concept that originated from semiconductors. It is formed when two materials with different chemical potentials are brought into contact with each other and the charge carriers in two materials cannot migrate to establish local charge neutrality. Theoretically, both electrons and atoms would be driven to the material with the lowest chemical potential near the interphase. However, the insulating nature of solid electrolytes makes it difficult for electrons to transport. The only charge carrier between the electrolyte and electrode in ASSLBs is Li⁺, which creates a space charge layer^[163,164].

The role that the space charge layer plays in the interphase between solid electrolyte/cathode can be controversial. In the early research on the interphase between cathodes and solid electrolytes, space charge layers have been indicated to be several micrometers in thickness, which would cause an enormous interphase resistance. Recently, Wang *et al.*^[165] characterized the LiCoO₂/Li₆PS₅Cl interphase by *in-situ* differential phase contrast scanning transmission electron microscopy (DPC-STEM) to investigate the net-charge-density distribution. It was found that a Li⁺ deficient negative-charge-density region would form once the LiCoO₂ cathode and Li₆PS₅Cl came into contact on the Li₆PS₅Cl side of the interphase. The STEM

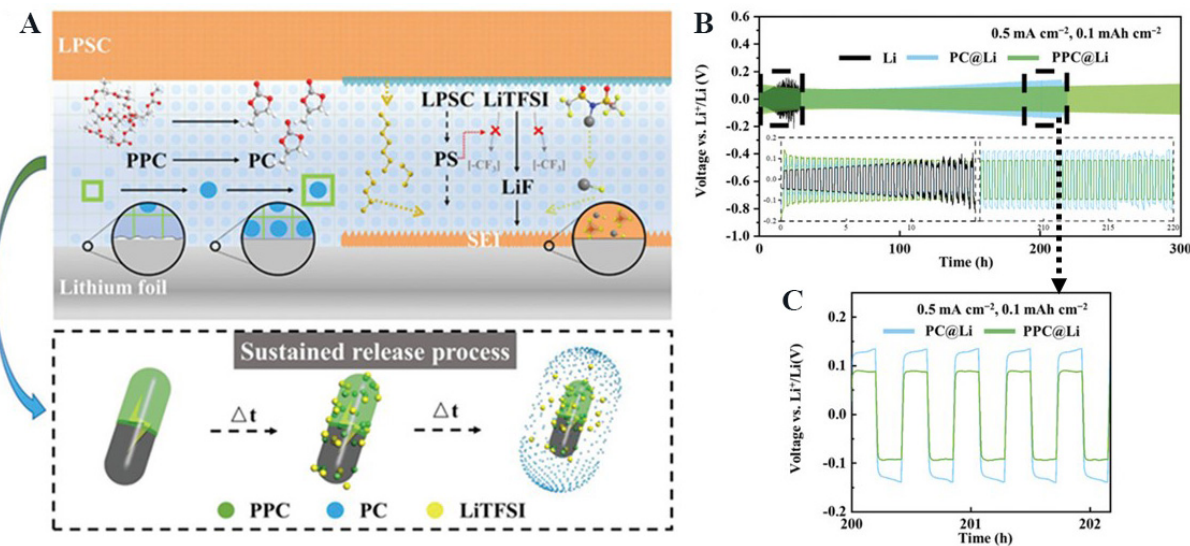


Figure 16. (A) Schematic illustration of *in situ* sustained release effect of poly(propylene carbonate) between $\text{Li}_6\text{PS}_5\text{Cl}$ and Li anode. (B, C) Galvanostatic discharge/charge voltage profiles of $\text{Li}/\text{Li}_6\text{PS}_5\text{Cl}/\text{Li}$ (Li) and PPC@Li/ $\text{Li}_6\text{PS}_5\text{Cl}/\text{PPC}@\text{Li}$ (PPC@Li) symmetric cells at a current density of 0.5 mA cm^{-2} and a cut-off capacity of 0.1 mAh cm^{-2} at RT. Reproduced with permission^[161] (Copyright 2020, Wiley-VCH). RT: Room temperature.

image of pristine $\text{LiCoO}_2/\text{Li}_6\text{PS}_5\text{Cl}$ interphase displayed that the space charge layer was about several nanometers in thickness, which was an order of magnitude thinner than previously expected. Furthermore, in the process of studying the Li^+ kinetics by solid-state nuclear magnetic resonance (SS-NMR), Yu *et al.*^[166] surprisingly concluded that interphase resistances were only a few $\Omega \text{ cm}^{-2}$ over pristine electrode-electrolyte interphases. This favored the observation that the thickness of space charge layer was on the nanometer scale since such a thickness was unlikely to lead to a notable interphase resistance.

A recent study by Niek *et al.*^[163] might put an end to the debate. They proposed a simple model to simulate the interphase capacitance and resistance caused by the space charge layer. This model is applied to LiCoO_2 in contact with LLZO ($\text{Li}_7\text{La}_3\text{Zr}_2\text{O}_{12}$) and LATP [$\text{Li}_{1.2}\text{Al}_{0.2}\text{Ti}_{1.8}(\text{PO}_4)_3$] solid electrolytes at several voltages. The results of the prediction demonstrated that the resistance of the space charge layer is negligible, except for the situation that layers completely depleted of Li^+ are formed in solid electrolytes. For the interphase between LiCoO_2 and $\text{Li}_6\text{PS}_5\text{Cl}$, the formation of layers completely depleted of Li^+ was observed by DPC-STEM at a bias voltage of 2.2 V, which hindered the transport of Li^+ to the cathode and increased the interphase resistance^[165]. Therefore, the space charge layer could influence the sulfide/cathode interphase and should be considered when designing a proper electrolyte/electrode interphase.

Interfacial reactions

The interfacial reactions at the cathode/sulfide interphase mainly originate from sulfur. According to a first-principles study on the electrochemical window of sulfide electrolytes, the onset oxidation potential of sulfides was predicted to $\sim 2.0\text{--}2.3 \text{ V}$ (vs. Li^+/Li) due to the existence of S element^[146]. For this reason, severe side reactions between sulfide and cathode would always occur during the process of charging. The oxidation of sulfide electrolytes near the cathode intends to form an ionic insulating layer to block the transport of Li^+ , which in turn enhances the interphase resistance. Furthermore, the side reactions between sulfide and high-voltage oxide cathodes sometimes destroy the crystalline structure of oxides, resulting in an irreversible capacity loss^[167].

Koerver *et al.*^[168] presented a detailed study that revealed the interphase between an NMC811 cathode and β -Li₃PS₄ electrolyte by utilizing XPS and *in-situ* EIS. According to the discussion of reaction mechanism, they proposed that β -Li₃PS₄ electrolyte might be polymerized into Li₂P₂S₆, Li₄P₂S₇ and Li₄P₂S₈. Based on the results of XPS characterization, the redox activity of Li₆PS₅Cl in ASSLBs was investigated by Zhang *et al.*^[169]. It was revealed that Li₆PS₅Cl would be oxidized into P₂S₅, LiCl and polysulfides in the cathode. Additionally, a LiCoO₂ cathode intended to react with Li₆PS₅Cl to produce phosphate upon cycling. Auvergniot *et al.*^[170] then also carried out further research on the interphase stability of Li₆PS₅Cl towards different oxide cathodes. The XPS results displayed that P₂S₅, LiCl, phosphate and polysulfides were the general reaction products of oxide cathodes and the Li₆PS₅Cl electrolyte. Interestingly, the side reactions did not severely hinder the good cyclability of batteries since Li₆PS₅Cl could contribute to the reversible capacity. Moreover, Zheng *et al.*^[171] unraveled the electrochemical stability of Li₁₀SnP₂S₁₂ in ASSLBs via solid-state NMR and XPS. It was demonstrated that Li₁₀SnP₂S₁₂ suffered from severe side reactions when preparing cathode composites by ball-milling. As shown in Figure 17A-C, the broad Li⁺ peak indicated the generation of low ionic conductivity species. By the confirmation of ³¹P and ¹¹⁹Sn spectra in Figure 17B and C, Li₃PS₄ and Li₄SnS₄ would form when ball-milling Li₁₀SnP₂S₁₂ electrolytes and LiCoO₂ together [Figure 17D]. The detailed XPS investigation then indicated that Li₁₀SnP₂S₁₂ oxidized into S, SnS₂ and P₂S₅ when the ASSLBs were charged to 4.2 V. Though the interfacial reactions of sulfides on the cathodic sides may provide extra capacity, the initial low CE and the generation of low ionic conductivity species are detrimental to the electrochemical performance of ASSLBs. Thus, an appropriate method to protect sulfides from being constantly oxidized by cathodes is desperately required.

Mechanical instability

The contact between particles has always been a dilemma for the cathode of ASSLBs. Several kinds of solid/solid interphases, including cathode/cathode, cathode/electrolyte, cathode/electron conductor (carbon) and electrolyte/electron conductor (carbon), can initially form upon mixing the components of cathode together. The existence of various interphases on the cathode creates an arduous condition for the transport and exchange of ions and electrons. The insufficient solid/solid contact increases the interfacial resistance. During the process of charging and discharging, accompanied side reactions generate species of low ionic conductivity, which block the contact between cathode particles and sulfide electrolytes^[171]. In addition, introducing an electron conductor to the cathode composite intends to strengthen the side reactions of sulfides^[172]. Though the overall electron conductivity may be enhanced, the contact loss between sulfides and cathode particles hinders the diffusion of Li⁺. Furthermore, the volume of cathode particles would expand or shrink when processing charging or discharging, which destroys the ionic- or electronic-conducting network^[173]. The issue of volume expansion shrinking is especially severe in Li-S ASSLBs due to the violent volume difference between S particles and Li₂S. After long cycles, the accumulated side reactions induce the pulverization of cathode particles. For this reason, the complete crystal structure of the cathode is broken, which irreversibly decreases the capacity of ASSLBs^[174].

Interfacial engineering

Due to the above-mentioned problems that exist in sulfide/cathode interphases, it is imperative to design an appropriate structure of a cathode composite. Synthesizing a relatively stable electrolyte against cathode particles is an alternative perspective. Wang *et al.*^[175] found the correlation between the performance of ASSLBs with the sulfides having the same stoichiometry but different crystallinity. It was reported that glass/glass-ceramic sulfides displayed better electrochemical performances rather than crystalline sulfides due to reduced occurrence of contact loss. The crystalline sulfides possessing high partial electronic conductivity may be the reason for severe degradation in the cathode composite. Even with the same stoichiometry, the electrochemical and mechanical properties of sulfides can be different. Therefore, a considerable selection for sulfides with satisfactory electrochemical and mechanical properties would benefit

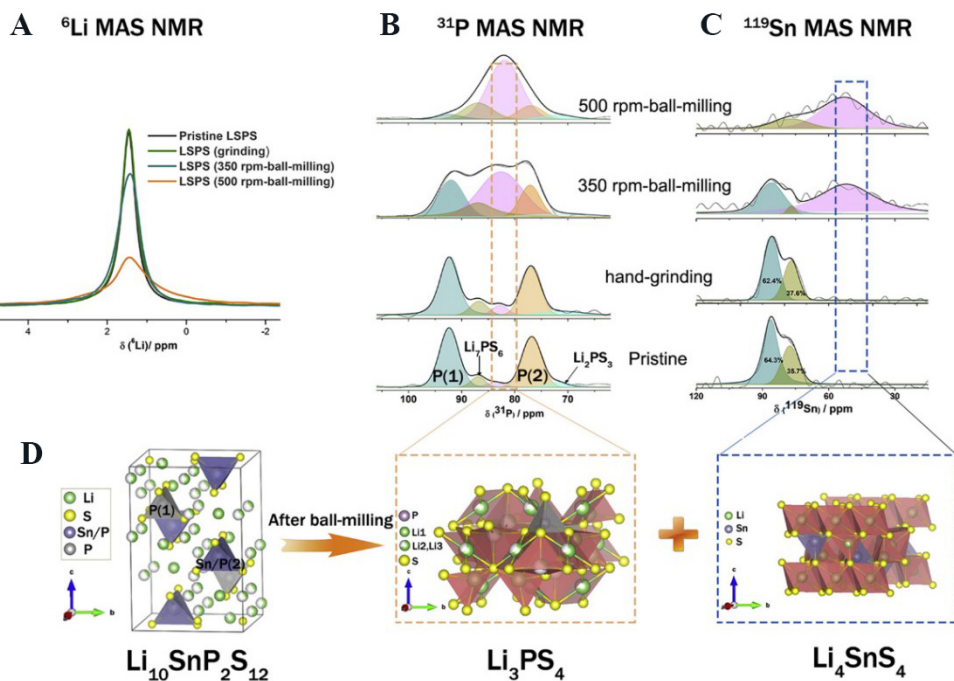


Figure 17. Solid-state NMR results of $\text{Li}_{10}\text{SnP}_2\text{S}_{12}$ before and after treatment. (A) ${}^6\text{Li}$, (B) ${}^{31}\text{P}$ and (C) ${}^{119}\text{Sn}$ MAS NMR spectra of $\text{Li}_{10}\text{SnP}_2\text{S}_{12}$ powder with different treatments. (D) Decomposition mechanism of $\text{Li}_{10}\text{SnP}_2\text{S}_{12}$ powder after ball-milling. Reproduced with permission^[171] (Copyright 2019, Elsevier).

the optimization of cathode composites.

In addition, Zhang *et al.*^[172] found that the introduction of carbon into a cathode composite might have detrimental effects on the electrochemical performance. The cathode composite incorporated with LGPS electrolytes and carbon exhibited more severe degradation and larger volume change compared to the composite without carbon. Analysis by XPS indicated that carbon fastened the decomposition of sulfides by transferring the Li of low chemical potential in the charged state deeper into the electrolytes and expanding the decomposition region. Therefore, in their later work, a non-carbon $\text{LiNi}_{0.7}\text{Co}_{0.1}\text{Mn}_{0.2}\text{O}_2$ (NCM622) cathode composite was proposed. It was surprisingly detected that the crystal of NCM622 displayed a certain level of electronic conductivity. By carefully controlling the ratio of $\text{Li}_6\text{PS}_5\text{Cl}$ and NCM622 without adding extra electronic conductors, both the ionic and the electronic conductivity of the cathode composite met the standards for normal application^[173]. Recently, Liu *et al.*^[173] presented in-depth research on the effects of the size and crystallinity of $\text{LiNi}_{0.8}\text{Co}_{0.1}\text{Mn}_{0.1}\text{O}_2$ (NCM811) cathodes on the electrochemical performance. By combining the characterization methods of XPS, solid-NMR, *in-situ* EIS and focused ion beam-SEM, the electrochemical performance and electrochemomechanical behavior of polycrystalline NCM811, small-sized polycrystalline NCM811 and single-crystal NCM811 in $\text{Li}_{10}\text{SnP}_2\text{S}_{12}$ -based ASSBs were compared. It was found that single-crystal NCM811 with good microstructural integrity performed better than polycrystalline and small-sized polycrystalline NCM811. However, the mechanism of the extraordinary performance of single-crystal NCM811 remains to be discovered.

As well as tuning the crystallinity of cathodes and electrolytes, coating a protective layer on cathode particles is a more common method to realize the reversible charging-discharging behavior of the cathode. Typically, LiNbO_3 -coated LiCoO_2 was widely used as cathode materials in recent work. LiNbO_3 with high ionic conductivity, low electronic conductivity and relatively wide electrochemical window worked well as a

buffer layer. The resistance of the cathode composite incorporating LiNbO_3 -coated LiCoO_2 was reduced and the side reactions were also prohibited. To realize high energy density in ASSLBs, Ni-rich oxide cathodes should be considered. Constructing a buffer layer on Ni-rich oxide cathodes is also proved to be effective to enhance electrochemical performance. Recently, Li *et al.*^[177] successfully prepared LiNbO_3 -coated NCM811 cathodes, with 1 wt.% LiNbO_3 -coated NCM811 cathodes demonstrated a high initial discharge capacity of 203 mAh g⁻¹ and excellent rate performance. Peng *et al.*^[178] carried out an in-depth investigation on coating $\text{LiNi}_{0.7}\text{Co}_{0.1}\text{Mn}_{0.2}\text{O}_2$ (NCM712) with LiNbO_3 . The LiNbO_3 -coated NCM712 delivered an initial discharge capacity of 80.9 mAh g⁻¹ at 5 C at RT with a capacity retention of 87.5% after 600 cycles. The coating effectively suppressed the volume change of cathode particles during cycling and prohibited the side reactions, which was confirmed by the results of XPS and TEM.

Moreover, Banerjee *et al.*^[179] investigated the interfacial reactions between $\text{Li}_6\text{PS}_5\text{Cl}$ and $\text{LiNi}_{0.85}\text{Co}_{0.1}\text{Al}_{0.05}\text{O}_2$ (NCA) by ab-initio molecular dynamics. It was found by radical distribution functions that PO_4^{3-} polyhedra form after cycling [Figure 18B and C]. The LiNbO_3 coating on NCA cathodes could effectively improve the thermodynamic stability between NCA and $\text{Li}_6\text{PS}_5\text{Cl}$ by lowering the exothermic reaction energy [Figure 18A]. The initial charge plateau previously observed between 2.3 and 3.6 V at the 1st cycle vanished at the 2nd cycle in the ASSLBs using LNO-coated NCA, which confirmed that LNO could prevent the electrolytes from decomposing [Figure 18D]. As a consequence, the ASSLBs exhibited excellent cycling stability with a capacity retention of 93% at 100 cycles [Figure 18E]. Li *et al.*^[180] constructed a nanoscale LATP protective layer on single-crystal $\text{LiNi}_{0.6}\text{Co}_{0.2}\text{Mn}_{0.2}\text{O}_2$ (NCM622). The conformal LATP buffer layer with high-voltage stability decreased the oxidation decomposition of sulfides. The ASSLBs incorporated with LATP-coated single-crystal NCM622 presented a discharge capacity of 152.1 mAh g⁻¹ with a capacity retention of 87.6% after 100 cycles at 0.1 C.

Aside from building a buffer layer on cathodes, Wang *et al.*^[181] noticed that the incompatibility of sulfides and oxide cathodes could be eliminated by doping sulfur into the crystal structure of $\text{LiNi}_{0.5}\text{Mn}_{1.5}\text{O}_4$ (LNMO). Compared with surface coatings, this new perspective required less arduous operation. Moreover, the ionic conductivity of LNMO particles was significantly improved by the introduction of sulfur. The S-doped LNMO/sulfide ASSLBs delivered a three-times higher initial discharge capacity and much higher capacity retention than the bare LNMO counterpart.

FABRICATION OF ASSLBS WITH HIGH CELL-LEVEL ENERGY DENSITY

Based on Ohm's law, the internal resistance of a battery is proportional to the Ohmic polarization when the current is constant. Considering that commercialized batteries are cycled at a relatively large current density in the actual application scenario, the electrolyte with high resistance will cause the proportion of Ohmic polarization to increase rapidly. Thus, employing electrolytes with low overall resistance in ASSLBs is a major concern.

The thickness and ionic conductivity of electrolytes are negatively proportional to the resistance. According to this, an ideal interlayer should be thin and of high ionic conductivity. Randau *et al.*^[182] proposed a benchmark for the performance of ASSLBs recently. It was mentioned that the thickness of the thiophosphate solid electrolyte separator should be less than 40 μm under the condition that the area capacity of NCM cathode was 5 mAh cm⁻² and the thickness of Li metal was 20 μm if the energy density of ASSLBs with NCM as cathodes is required to exceed 400 Wh kg⁻¹. However, the practical energy density of sulfide-based ASSLBs has not exceeded 200 Wh kg⁻¹. Either increasing the ratio of cathodes or decreasing the thickness of the interlayer would help to enhance the energy density. The high ionic conductivity of sulfide endows the potential of its application in the field of high energy-density ASSLBs. By the slurry

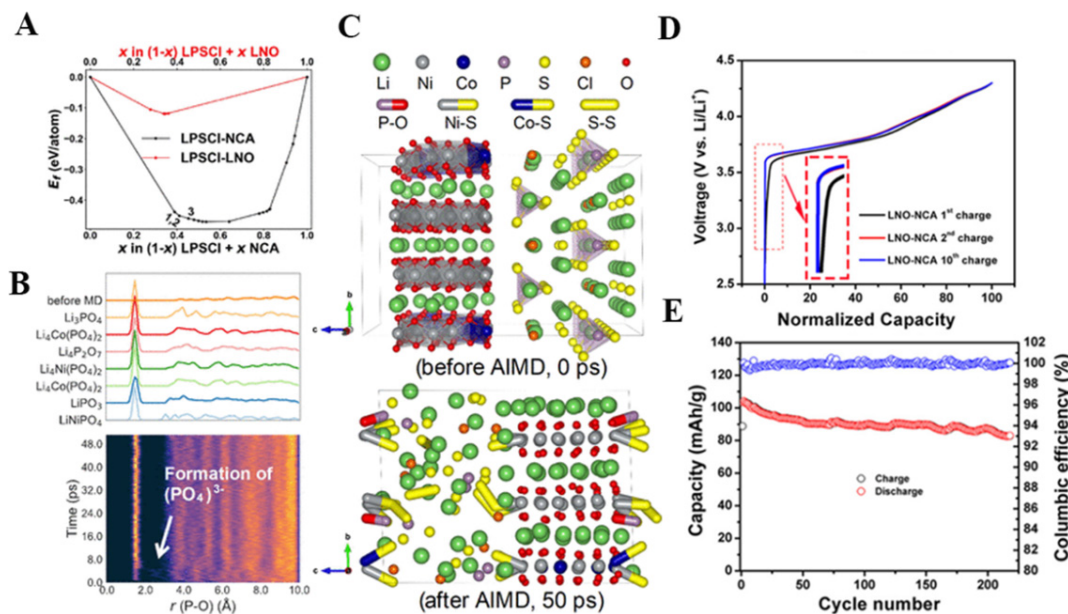


Figure 18. (A) Pseudo-binary phase diagram between $\text{Li}_6\text{PS}_5\text{Cl}$ electrolyte and discharged NCA cathode at different mixing ratios, the red line indicates the case with LiNbO_3 coating. (B) Atomic structure of the half-charged NCA/ $\text{Li}_6\text{PS}_5\text{Cl}$ interface at 0 and 50 ps, which summarizes the key observations in the ab-initio molecular dynamics (AIMD) simulation. (C) Visualization of the formation of characteristic PO bonds in PO_4 polyhedra at the half-charged NCA/ $\text{Li}_6\text{PS}_5\text{Cl}$ interface using RDF. The charging profile (D) of LPSCI and NCA-LPSCI ASSBs at the 1st, 2nd and 10 th cycles. Cycling stability of (E) ASSBs for LNO-coated and bare NCA at the rate of C/3.5. Reproduced with permission^[179] (Copyright 2019, American Chemical Society). NCA: $\text{LiNi}_{0.85}\text{Co}_{0.1}\text{Al}_{0.05}\text{O}_2$.

method, Wang *et al.*^[183] prepared a $\text{Li}_6\text{PS}_5\text{Cl}/\text{poly}(\text{vinylidene difluoride})$ composite free-standing membrane with a thickness of 100–120 μm . The ionic conductivity of the sulfide composite membrane was $1 \times 10^{-3} \text{ S cm}^{-1}$. Cycling stability of $\text{Li}_6\text{PS}_5\text{Cl}$ electrolyte against Li metal was improved after adding poly(1,1-difluoroethylene) (PVDF), which was proved by longer cycling life and lower polarization of symmetric cell using the composite membrane as the interlayer in the galvanostatic tests at a current density of 0.2 mA cm^{-2} . Liu *et al.*^[184] coated a 5 nm thick homogeneous polydopamine layer on $\text{Li}_6\text{PS}_5\text{Cl}$ electrolyte and prepared a 35 μm thick free-standing electrolyte film by cold pressing the coated electrolytes. Zhu *et al.*^[185] designed a free-standing sulfide film through a self-limited strategy. By employing a chemically compatible cellulose membrane as the skeleton, the thickness of SSE films was defined and the mechanical strength was also improved.

Zhang *et al.*^[186] ball-milled a $\text{Li}_{5.4}\text{PS}_{4.4}\text{Cl}_{1.6}$ powder and polytetrafluoroethylene fiber to prepare a solid electrolyte membrane. The thickness of obtained sulfide membrane was 30 μm and the ionic conductivity of it exceeded $8 \times 10^{-3} \text{ S cm}^{-1}$, which basically satisfied the benchmark of high-energy-density ASSLBs [Figure 19A]. An Al_2O_3 interphase was introduced to avoid the direct contact between Li and membrane for the purpose of suppressing side reactions and dendrites growth. Consequently, the ASSLBs configured with Al_2O_3 -coated-Li/sulfide membrane/NCM exhibited capacity retention of 80.2% after 150 cycles with a high NCM mass loading of 11.6 mg cm^{-2} at 0.05 C [Figure 19B and C]. Moreover, Samsung fabricated a thin sulfide film using a doctor blade^[154]. By modifying the composition and structure of anode and cathode, a 900 Wh L^{-1} level ASSLBs with superior cycle life (> 1000 times) was obtained. Very recently, Xu *et al.*^[187] developed a water-stable sulfide membrane by spray coating LATP nanoparticles and fluorinated polysiloxane. The as-prepared coating can help sulfide membrane withstand extreme exposure conditions with water jetting in the ambient environment, which brings down to the large-scale production of sulfide-based ASSLBs in the future.

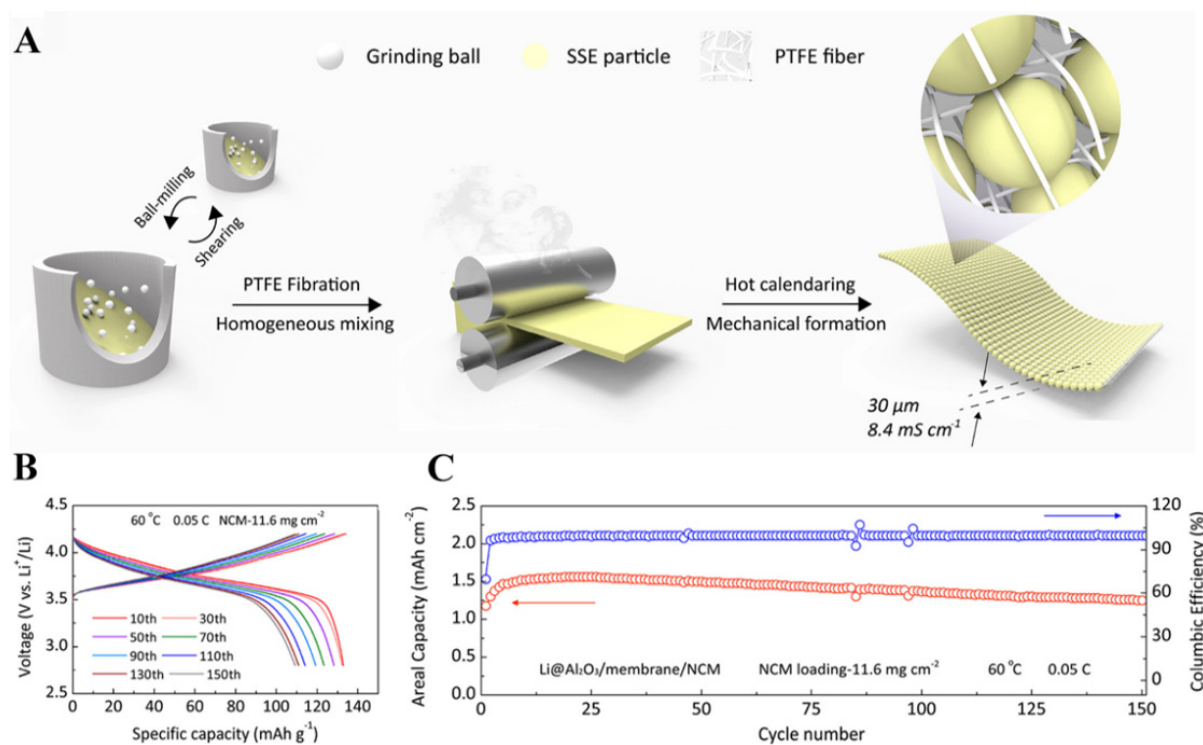


Figure 19. (A) Schematic illustration of ultrathin membrane fabrication. (B) Voltage profile and (C) cyclic performance of the NCM/Li ASSLBs with a high NCM mass loading of 11.6 mg cm^{-2} at 0.05 C (0.085 mA cm^{-2}). Reproduced with permission^[186] (Copyright 2021, American Chemical Society).

SUMMARY AND OUTLOOK

As a hot research topic in recent years, solid electrolytes are recognized as being pivotal to the next-generation energy storage field due to their non-flammable properties and high Li^+ migration number. Among all the solid electrolytes, sulfides are proposed to be a promising family of materials due to their high ionic conductivity and good wettability with Li metal. Either glass, glass-ceramic or crystalline sulfide electrolytes have demonstrated their possibility to be applied as interlayers in ASSLBs. For glass and glass-ceramic sulfides, almost infinite possibilities are provided for altering their chemistry to obtain the desired properties. Although many of the facets of crystalline sulfides have been revealed, the mechanistic research by DFT has provided several theoretical guidance for designing crystalline sulfide electrolytes with ultrahigh ionic conductivity. Moreover, the synthesizing approaches of sulfides required fewer effort than that of oxide electrolytes. In particular, the liquid-phase synthesis approach is promising for large-scale industrialization. Furthermore, the high ionic conductivity of sulfides endows the potential of its application in the field of high energy-density ASSLBs. Cell-level high energy density sulfide-based ASSLBs with thin-film interlayers have come to reality.

Nonetheless, the S atoms in sulfides are sensitive to humid air. Consequently, H_2S -generation is inevitable when preparing sulfides outside the Ar-filled glove box. This drawback prevents the large-scale production of sulfides. Luckily, with the in-depth research on sulfides proceeding, some methods to improve the stability of sulfides to humid air have been discovered.

The sharp electrochemical window of sulfides leads to severe side reactions both on the cathode and anode sides. The side reactions between Li and electrolytes lead to the drop of CE and hinder the development of

high-energy-density LMBs. The oxidation of sulfide electrolytes near the cathode intends to form an ionic insulating layer to block the transport of Li^+ , which in turn enhances the interphase resistance. In order to develop ASSLBs with long cycling life and high capacity retention, the influence of side reactions should be decreased to an ignorable level.

Dendrite growth is still major issue in sulfide-based electrolytes and the contact loss between Li/sulfides even deteriorates the situation. The compositional tuning of anodes and electrolytes and the construction of SEIs and interlayers have been proposed to solve the dilemma. At present, the highest CCD value of symmetric sulfide-based Li/Li cells could reach a level comparable to that of LMBs using organic electrolytes. With the combination of experimental results and theoretical study, practical criteria are built and would provide the guidance for further research on developing stable interphase between Li and sulfides.

The mechanical instability of sulfides hinders the complete charging/discharging behaviors of cathode materials while the formed space charge layer increases the interfacial resistance by hindering the transport of charge carriers. Detailed research into the properties of sulfide and cathode particles optimized the preparation methodology of cathode composites. Moreover, coating a protective layer on cathode particles is a more common method to realize the reversible charging-discharging behaviors of the cathode. Particularly, the method of mixing raw materials in a liquid phase is proposed as an alternative to mechanical mixing.

The recent progress of sulfide electrolytes for ASSLBs may provide guidance for future research. First of all, investigating the mechanism of improving the ionic conductivity of sulfide electrolytes will definitely create more candidates for the practical interlayer in ASSLBs. Secondly, in order to satisfy the needs of mass production, novel methods should be proposed to enhance the air stability of sulfide electrolytes. Moreover, the interphase problems constrain the electrochemical performances of sulfide-based ASSLBs. It is true that a lot of the strategies to modify the interphase of sulfide/cathode and sulfide/anode are proved to be effective. The next target of interphase modification should be focused on practicality. Finally, though the ionic conductivity of sulfides is the highest among solid electrolytes, it is also necessary to reduce the thickness of the interlayer to obtain high energy density ASSLBs. For this reason, future work should focus on improving the electrochemical performances of ASSLBs with high cell-level energy density.

DECLARATIONS

Authors' contributions

Conceived the manuscript: Su H, Jiang Z

Wrote the manuscript: Su H, Jiang Z

Reviewed the manuscript: Tu J, Su H

Contributed to the discussion of the manuscript: Su H, Jiang Z, Liu Y, Li J, Gu C, Wang X, Xia X, Tu J

Availability of data and materials

Not applicable.

Financial support and sponsorship

This work is supported by the National Natural Science Foundation of China (No. U20A20126, 51971201) and Development Program of Zhejiang Province (2021C01175).

Conflicts of interest

All authors declared that there are no conflicts of interest.

Ethical approval and consent to participate

Not applicable.

Consent for publication

Not applicable.

Copyright

© The Author(s) 2022.

REFERENCES

1. Armand M, Tarascon JM. Building better batteries. *Nature* 2008;451:652-7. [DOI](#) [PubMed](#)
2. Zhang Q, Cao D, Ma Y, Natan A, Aurora P, Zhu H. Sulfide-based solid-state electrolytes: synthesis, stability, and potential for all-solid-state batteries. *Adv Mater* 2019;31:e1901131. [DOI](#) [PubMed](#)
3. Xu R, Zhang S, Wang X, et al. Recent developments of all-solid-state lithium secondary batteries with sulfide inorganic electrolytes. *Chemistry* 2018;24:6007-18. [DOI](#) [PubMed](#)
4. Chen S, Xie D, Liu G, et al. Sulfide solid electrolytes for all-solid-state lithium batteries: structure, conductivity, stability and application. *Energy Stor Mater* 2018;14:58-74. [DOI](#)
5. Banerjee A, Wang X, Fang C, Wu EA, Meng YS. Interfaces and interphases in all-solid-state batteries with inorganic solid electrolytes. *Chem Rev* 2020;120:6878-933. [DOI](#) [PubMed](#)
6. Zhang Z, Shao Y, Lotsch B, et al. New horizons for inorganic solid state ion conductors. *Energy Environ Sci* 2018;11:1945-76. [DOI](#)
7. Gao Z, Sun H, Fu L, et al. Promises, challenges, and recent progress of inorganic solid-state electrolytes for all-solid-state lithium batteries. *Adv Mater* 2018;30:e1705702. [DOI](#) [PubMed](#)
8. Jiang Z, Liang T, Liu Y, et al. Improved ionic conductivity and Li dendrite suppression capability toward $\text{Li}_7\text{P}_3\text{S}_{11}$ -based solid electrolytes triggered by Nb and O cosubstitution. *ACS Appl Mater Interfaces* 2020;12:54662-70. [DOI](#) [PubMed](#)
9. Hayashi A, Muramatsu H, Ohtomo T, Hama S, Tatsumisago M. Improvement of chemical stability of Li_3PS_4 glass electrolytes by adding M_xO_y ($\text{M} = \text{Fe}, \text{Zn}, \text{and Bi}$) nanoparticles. *J Mater Chem A* 2013;1:6320. [DOI](#)
10. Kato Y, Hori S, Saito T, et al. High-power all-solid-state batteries using sulfide superionic conductors. *Nat Energy* 2016;1. [DOI](#)
11. Zhou L, Assoud A, Zhang Q, Wu X, Nazar LF. New family of argyrodite thioantimonate lithium superionic conductors. *J Am Chem Soc* 2019;141:19002-13. [DOI](#) [PubMed](#)
12. Patel SV, Banerjee S, Liu H, et al. Tunable lithium-ion transport in mixed-halide argyrodites $\text{Li}_{6-x}\text{PS}_{5-x}\text{ClBr}_x$: an unusual compositional space. *Chem Mater* 2021;33:1435-43. [DOI](#)
13. Wu J, Liu S, Han F, Yao X, Wang C. Lithium/sulfide all-solid-state batteries using sulfide electrolytes. *Adv Mater* 2021;33:e2000751. [DOI](#) [PubMed](#)
14. Bachman JC, Muy S, Grimaud A, et al. Inorganic solid-state electrolytes for lithium batteries: mechanisms and properties governing ion conduction. *Chem Rev* 2016;116:140-62. [DOI](#) [PubMed](#)
15. Zhu Y, Mo Y. Materials design principles for air-stable lithium/sodium solid electrolytes. *Angew Chem Int Ed Engl* 2020;59:17472-6. [DOI](#) [PubMed](#)
16. Minami K, Mizuno F, Hayashi A, Tatsumisago M. Lithium ion conductivity of the $\text{Li}_2\text{S}-\text{P}_2\text{S}_5$ glass-based electrolytes prepared by the melt quenching method. *Solid State Ionics* 2007;178:837-41. [DOI](#)
17. Hayashi A, Minami K, Mizuno F, Tatsumisago M. Formation of Li^+ superionic crystals from the $\text{Li}_2\text{S}-\text{P}_2\text{S}_5$ melt-quenched glasses. *J Mater Sci* 2008;43:1885-9. [DOI](#)
18. Seino Y, Ota T, Takada K, Hayashi A, Tatsumisago M. A sulphide lithium super ion conductor is superior to liquid ion conductors for use in rechargeable batteries. *Energy Environ Sci* 2014;7:627-31. [DOI](#)
19. Xu R, Xia X, Yao Z, Wang X, Gu C, Tu J. Preparation of $\text{Li}_7\text{P}_3\text{S}_{11}$ glass-ceramic electrolyte by dissolution-evaporation method for all-solid-state lithium ion batteries. *Electrochimi Acta* 2016;219:235-40. [DOI](#)
20. Xu R, Wang X, Zhang S, et al. Rational coating of $\text{Li}_7\text{P}_3\text{S}_{11}$ solid electrolyte on MoS_2 electrode for all-solid-state lithium ion batteries. *J Power Sources* 2018;374:107-12. [DOI](#)
21. Ito S, Nakakita M, Aihara Y, Uehara T, Machida N. A synthesis of crystalline $\text{Li}_7\text{P}_3\text{S}_{11}$ solid electrolyte from 1,2-dimethoxyethane solvent. *J Power Sources* 2014;271:342-5. [DOI](#)
22. Liu Z, Fu W, Payzant EA, et al. Anomalous high ionic conductivity of nanoporous $\beta\text{-Li}_3\text{PS}_4$. *J Am Chem Soc* 2013;135:975-8. [DOI](#) [PubMed](#)
23. Yubuchi S, Uematsu M, Deguchi M, Hayashi A, Tatsumisago M. Lithium-ion-conducting argyrodite-type $\text{Li}_6\text{PS}_5\text{X}$ ($\text{X} = \text{Cl}, \text{Br}, \text{I}$) solid electrolytes prepared by a liquid-phase technique using ethanol as a solvent. *ACS Appl Energy Mater* 2018;1:3622-9. [DOI](#)
24. Song YB, Kim DH, Kwak H, et al. Tailoring solution-processable Li argyrodites $\text{Li}_{6+x}\text{P}_{1-x}\text{M}_x\text{S}_5\text{I}$ ($\text{M} = \text{Ge}, \text{Sn}$) and their microstructural evolution revealed by cryo-TEM for all-solid-state batteries. *Nano Lett* 2020;20:4337-45. [DOI](#) [PubMed](#)

25. Jung WD, Kim JS, Choi S, et al. Superionic halogen-rich Li-argyrodites using in situ nanocrystal nucleation and rapid crystal growth. *Nano Lett* 2020;20:2303-9. [DOI](#) [PubMed](#)
26. Fukushima A, Hayashi A, Yamamura H, Tatsumisago M. Mechanochemical synthesis of high lithium ion conducting solid electrolytes in a $\text{Li}_2\text{S}-\text{P}_2\text{S}_5-\text{Li}_3\text{N}$ system. *Solid State Ionics* 2017;304:85-9. [DOI](#)
27. Boulineau S, Courty M, Tarascon J, Viallet V. Mechanochemical synthesis of Li-argyrodite $\text{Li}_6\text{PS}_5\text{X}$ ($\text{X}=\text{Cl}, \text{Br}, \text{I}$) as sulfur-based solid electrolytes for all solid state batteries application. *Solid State Ionics* 2012;221:1-5. [DOI](#)
28. Jiang Z, Peng H, Liu Y, et al. A Versatile $\text{Li}_{6.5}\text{In}_{0.25}\text{P}_{0.75}\text{S}_5\text{I}$ sulfide electrolyte triggered by ultimate-energy mechanical alloying for all-solid-state lithium metal batteries. *Adv Energy Mater* 2021;11:2101521. [DOI](#) [PubMed](#)
29. Mizuno F, Hayashi A, Tadanaga K, Tatsumisago M. New, highly ion-conductive crystals precipitated from $\text{Li}_2\text{S}-\text{P}_2\text{S}_5$ glasses. *Adv Mater* 2005;17:918-21. [DOI](#)
30. Tao Y, Chen S, Liu D, Peng G, Yao X, Xu X. Lithium superionic conducting oxysulfide solid electrolyte with excellent stability against lithium metal for all-solid-state cells. *J Electrochem Soc* 2015;163:A96-101. [DOI](#)
31. Hayashi A, Hama S, Minami T, Tatsumisago M. Formation of superionic crystals from mechanically milled $\text{Li}_2\text{S}-\text{P}_2\text{S}_5$ glasses. *Electrochem commun* 2003;5:111-4. [DOI](#)
32. Jiang Z, Li Z, Wang X, Gu C, Xia X, Tu J. Robust $\text{Li}_6\text{PS}_5\text{I}$ interlayer to stabilize the tailored electrolyte $\text{Li}_{9.95}\text{SnP}_2\text{S}_{11.95}\text{F}_{0.05}/\text{Li}$ metal interface. *ACS Appl Mater Interfaces* 2021;13:30739-45. [DOI](#) [PubMed](#)
33. Adeli P, Bazak JD, Park KH, et al. Boosting solid-state diffusivity and conductivity in lithium superionic argyrodites by halide substitution. *Angew Chem Int Ed Engl* 2019;58:8681-6. [DOI](#) [PubMed](#)
34. Liu Y, Peng H, Su H, et al. Ultrafast synthesis of I-rich lithium argyrodite glass-ceramic electrolyte with high ionic conductivity. *Adv Mater* 2022;34:e2107346. [DOI](#) [PubMed](#)
35. Xu R, Xia X, Wang X, Xia Y, Tu J. Tailored $\text{Li}_2\text{S}-\text{P}_2\text{S}_5$ glass-ceramic electrolyte by MoS_2 doping, possessing high ionic conductivity for all-solid-state lithium-sulfur batteries. *J Mater Chem A* 2017;5:2829-34. [DOI](#)
36. Mercier R, Malugani J, Fahys B, Robert G. Superionic conduction in $\text{Li}_2\text{S}-\text{P}_2\text{S}_5-\text{LiI}$ -glasses. *Solid State Ionics* 1981;5:663-6. [DOI](#)
37. Teragawa S, Aso K, Tadanaga K, Hayashi A, Tatsumisago M. Liquid-phase synthesis of a Li_3PS_4 solid electrolyte using N-methylformamide for all-solid-state lithium batteries. *J Mater Chem A* 2014;2:5095. [DOI](#)
38. Phuc NHH, Totani M, Morikawa K, Muto H, Matsuda A. Preparation of Li_3PS_4 solid electrolyte using ethyl acetate as synthetic medium. *Solid State Ionics* 2016;288:240-3. [DOI](#)
39. Calpa M, Rosero-navarro NC, Miura A, Tadanaga K. Instantaneous preparation of high lithium-ion conducting sulfide solid electrolyte $\text{Li}_7\text{P}_3\text{S}_{11}$ by a liquid phase process. *RSC Adv* 2017;7:46499-504. [DOI](#)
40. Wang Y, Lu D, Bowden M, et al. Mechanism of formation of $\text{Li}_7\text{P}_3\text{S}_{11}$ solid electrolytes through liquid phase synthesis. *Chem Mater* 2018;30:990-7. [DOI](#)
41. Yubuchi S, Teragawa S, Aso K, Tadanaga K, Hayashi A, Tatsumisago M. Preparation of high lithium-ion conducting $\text{Li}_6\text{PS}_5\text{Cl}$ solid electrolyte from ethanol solution for all-solid-state lithium batteries. *J Power Sources* 2015;293:941-5. [DOI](#)
42. Rosero-navarro NC, Miura A, Tadanaga K. Preparation of lithium ion conductive $\text{Li}_6\text{PS}_5\text{Cl}$ solid electrolyte from solution for the fabrication of composite cathode of all-solid-state lithium battery. *J Sol-Gel Sci Technol* 2019;89:303-9. [DOI](#)
43. Zhou L, Park K, Sun X, et al. Solvent-engineered design of argyrodite $\text{Li}_6\text{PS}_5\text{X}$ ($\text{X}=\text{Cl}, \text{Br}, \text{I}$) solid electrolytes with high ionic conductivity. *ACS Energy Lett* 2019;4:265-70. [DOI](#)
44. Yubuchi S, Uematsu M, Hotehama C, Sakuda A, Hayashi A, Tatsumisago M. An argyrodite sulfide-based superionic conductor synthesized by a liquid-phase technique with tetrahydrofuran and ethanol. *J Mater Chem A* 2019;7:558-66. [DOI](#)
45. Hayashi A, Hama S, Morimoto H, Tatsumisago M, Minami T. Preparation of $\text{Li}_2\text{S}-\text{P}_2\text{S}_5$ amorphous solid electrolytes by mechanical milling. *J Am Ceram Soc* 2001;84:477-79. [DOI](#)
46. Shin BR, Nam YJ, Oh DY, Kim DH, Kim JW, Jung YS. Comparative study of TiS_2/Li -in all-solid-state lithium batteries using glass-ceramic Li_3PS_4 and $\text{Li}_{10}\text{GeP}_2\text{S}_{12}$ solid electrolytes. *Electrochimica Acta* 2014;146:395-402. [DOI](#)
47. Yamane H, Shibata M, Shimane Y, et al. Crystal structure of a superionic conductor, $\text{Li}_7\text{P}_3\text{S}_{11}$. *Solid State Ionics* 2007;178:1163-7. [DOI](#)
48. Zhao F, Liang J, Yu C, et al. A versatile Sn-substituted argyrodite sulfide electrolyte for all-solid-state Li metal batteries. *Adv Energy Mater* 2020;10:1903422. [DOI](#)
49. Liang J, Chen N, Li X, et al. $\text{Li}_{10}\text{Ge}(\text{P}_{1-x}\text{Sb}_x)_2\text{S}_{12}$ lithium-ion conductors with enhanced atmospheric stability. *Chem Mater* 2020;32:2664-72. [DOI](#)
50. Yi J, Chen L, Liu Y, Geng H, Fan LZ. High capacity and superior cyclic performances of all-solid-state lithium-sulfur batteries enabled by a high-conductivity $\text{Li}_{10}\text{SnP}_2\text{S}_{12}$ solid electrolyte. *ACS Appl Mater Interfaces* 2019;11:36774-81. [DOI](#) [PubMed](#)
51. Kamaya N, Homma K, Yamakawa Y, et al. A lithium superionic conductor. *Nat Mater* 2011;10:682-6. [DOI](#) [PubMed](#)
52. Park KH, Oh DY, Choi YE, et al. Solution-processable glass $\text{LiI-Li}_4\text{SnS}_4$ superionic conductors for all-solid-state Li-ion batteries. *Adv Mater* 2016;28:1874-83. [DOI](#) [PubMed](#)
53. Zhao BS, Wang L, Chen P, et al. Congener substitution reinforced $\text{Li}_7\text{P}_{2.9}\text{Sb}_{0.1}\text{S}_{10.75}\text{O}_{0.25}$ glass-ceramic electrolytes for all-solid-state lithium-sulfur batteries. *ACS Appl Mater Interfaces* 2021;13:34477-85. [DOI](#) [PubMed](#)
54. Rajagopal R, Ryu K. Structural investigations, visualization, and electrolyte properties of silver halide-doped $\text{Li}_7\text{P}_3\text{S}_{11}$ lithium superionic conductors. *ACS Sustainable Chem Eng* 2021;9:1105-17. [DOI](#)
55. Kaib T, Haddadpour S, Kapitein M, et al. New lithium chalcogenidotetrelates, LiChT : synthesis and characterization of the Li^+ -conducting tetralithium ortho-sulfidostannate Li_4SnS_4 . *Chem Mater* 2012;24:2211-9. [DOI](#)
56. Sahu G, Rangasamy E, Li J, et al. A high-conduction Ge substituted Li_3AsS_4 solid electrolyte with exceptional low activation energy.

- J Mater Chem A 2014;2:10396-403. DOI
57. Kanno R, Murayama M. Lithium ionic conductor thio-LISICON: the $\text{Li}_2\text{S}-\text{GeS}_2-\text{P}_2\text{S}_5$ system. *J Electrochem Soc* 2001;148:A742. DOI
58. Bron P, Johansson S, Zick K, Schmedt auf der Günne J, Dehnen S, Roling B. $\text{Li}_{10}\text{SnP}_2\text{S}_{12}$: an affordable lithium superionic conductor. *J Am Chem Soc* 2013;135:15694-7. DOI PubMed
59. Bron P, Dehnen S, Roling B. $\text{Li}_{10}\text{Si}_{0.3}\text{Sn}_{0.7}\text{P}_2\text{S}_{12}$ - a low-cost and low-grain-boundary-resistance lithium superionic conductor. *J Power Sources* 2016;329:530-5. DOI
60. Liu Y, Su H, Li M, et al. In situ formation of a Li_3N -rich interface between lithium and argyrodite solid electrolyte enabled by nitrogen doping. *J Mater Chem A* 2021;9:13531-9. DOI
61. Chen T, Zeng D, Zhang L, et al. Sn-O dual-doped Li-argyrodite electrolytes with enhanced electrochemical performance. *J Energy Chem* 2021;59:530-7. DOI
62. Dietrich C, Weber DA, Sedlmaier SJ, et al. Lithium ion conductivity in $\text{Li}_2\text{S}-\text{P}_2\text{S}_5$ glasses - building units and local structure evolution during the crystallization of superionic conductors Li_3PS_4 , $\text{Li}_7\text{P}_3\text{S}_{11}$ and $\text{Li}_4\text{P}_2\text{S}_7$. *J Mater Chem A* 2017;5:18111-9. DOI
63. Pradel A, Ribes M. Electrical properties of lithium conductive silicon sulfide glasses prepared by twin roller quenching. *Solid State Ionics* 1986;18-19:351-5. DOI
64. Zhang Z, Kennedy J. Synthesis and characterization of the $\text{B}_2\text{S}_3-\text{Li}_2\text{S}$, the $\text{P}_2\text{S}_5-\text{Li}_2\text{S}$ and the $\text{B}_2\text{S}_3-\text{P}_2\text{S}_5-\text{Li}_2\text{S}$ glass systems. *Solid State Ionics* 1990;38:217-24. DOI
65. Tatsumisago M, Hirai K, Minami T, Takada K, Kondo S. Superionic conduction in rapidly quenched $\text{Li}_2\text{S}-\text{SiS}_2-\text{Li}_3\text{PO}_4$ glasses. *J Ceram Soc Japan* 1993;101:1315-7. DOI
66. Tatsumisago M, Hirai K, Hirata T, Takahashi M, Minami T. Structure and properties of lithium ion conducting oxysulfide glasses prepared by rapid quenching. *Solid State Ionics* 1996;86-88:487-90. DOI
67. Wada H, Menetrier M, Levasseur A, Hagenmuller P. Preparation and ionic conductivity of new $\text{B}_2\text{S}_3-\text{Li}_2\text{S}-\text{LiI}$ glasses. *Mater Res Bull* 1983;18:189-93. DOI
68. Kennedy JH, Zhang Z, Eckert H. Ionically conductive sulfide-based lithium glasses. *J Non Cryst Solids* 1990;123:328-38. DOI
69. Yamauchi A, Sakuda A, Hayashi A, Tatsumisago M. Preparation and ionic conductivities of $(100-x)(0.75\text{Li}_2\text{S}-0.25\text{P}_2\text{S}_5)\cdot x\text{LiBH}_4$ glass electrolytes. *J Power Sources* 2013;244:707-10. DOI
70. Kudu ÖU, Famprikis T, Fleutot B, et al. A review of structural properties and synthesis methods of solid electrolyte materials in the $\text{Li}_2\text{S} - \text{P}_2\text{S}_5$ binary system. *J Power Sources* 2018;407:31-43. DOI
71. Mizuno F, Hayashi A, Tadanaga K, Tatsumisago M. High lithium ion conducting glass-ceramics in the system $\text{Li}_2\text{S}-\text{P}_2\text{S}_5$. *Solid State Ionics* 2006;177:2721-5. DOI
72. Dietrich C, Weber DA, Culver S, et al. Synthesis, structural characterization, and lithium ion conductivity of the lithium thiophosphate $\text{Li}_2\text{P}_2\text{S}_6$. *Inorg Chem* 2017;56:6681-7. DOI PubMed
73. Kim J, Yoon Y, Lee J, Shin D. Formation of the high lithium ion conducting phase from mechanically milled amorphous $\text{Li}_2\text{S}-\text{P}_2\text{S}_5$ system. *J Power Sources* 2011;196:6920-3. DOI
74. Trevey J, Jang JS, Jung YS, Stoldt CR, Lee S. Glass-ceramic $\text{Li}_2\text{S}-\text{P}_2\text{S}_5$ electrolytes prepared by a single step ball milling process and their application for all-solid-state lithium-ion batteries. *Electrochim commun* 2009;11:1830-3. DOI
75. Xu R, Xia X, Li S, Zhang S, Wang X, Tu J. All-solid-state lithium-sulfur batteries based on a newly designed $\text{Li}_7\text{P}_{2.9}\text{Mn}_{0.1}\text{S}_{10.7}\text{I}_{0.3}$ superionic conductor. *J Mater Chem A* 2017;5:6310-7. DOI
76. Kanno R. Synthesis of a new lithium ionic conductor, thio-LISICON-lithium germanium sulfide system. *Solid State Ionics* 2000;130:97-104. DOI
77. Seo I, Martin SW. Fast lithium ion conducting solid state thin-film electrolytes based on lithium thio-germanate materials. *Acta Materialia* 2011;59:1839-46. DOI
78. Kwak H, Park KH, Han D, Nam K, Kim H, Jung YS. Li^+ conduction in air-stable Sb-Substituted Li_4SnS_4 for all-solid-state Li-Ion batteries. *J Power Sources* 2020;446:227338. DOI
79. Sahu G, Lin Z, Li J, Liu Z, Dudney N, Liang C. Air-stable, high-conduction solid electrolytes of arsenic-substituted Li_4SnS_4 . *Energy Environ Sci* 2014;7:1053-8. DOI
80. Nishino S, Fujiwara T, Yamasaki H. Nanosecond quantum molecular dynamics simulations of the lithium superionic conductor $\text{Li}_{4-x}\text{Ge}_{1-x}\text{P}_x\text{S}_4$. *Phys Rev B* 2014;90:024303. DOI
81. Kuhn A, Duppel V, Lotsch BV. Tetragonal $\text{Li}_{10}\text{GeP}_2\text{S}_{12}$ and Li_7GePS_8 - exploring the Li ion dynamics in LGPS Li electrolytes. *Energy Environ Sci* 2013;6:3548. DOI
82. Mo Y, Ong SP, Ceder G. First principles study of the $\text{Li}_{10}\text{GeP}_2\text{S}_{12}$ lithium super ionic conductor material. *Chem Mater* 2012;24:15-7. DOI
83. Malik R, Burch D, Bazant M, Ceder G. Particle size dependence of the ionic diffusivity. *Nano Lett* 2010;10:4123-7. DOI PubMed
84. Kato Y, Saito R, Sakano M, Mitsui A, Hirayama M, Kanno R. Synthesis, structure and lithium ionic conductivity of solid solutions of $\text{Li}_{10}(1-\text{M})\text{P}_2\text{S}_{12}$ ($\text{M} = \text{Si}, \text{Sn}$). *J Power Sources* 2014;271:60-4. DOI
85. Ong SP, Mo Y, Richards WD, Miara L, Lee HS, Ceder G. Phase stability, electrochemical stability and ionic conductivity of the $\text{Li}_{10\pm 1}\text{MP}_2\text{X}_{12}$ ($\text{M} = \text{Ge}, \text{Si}, \text{Sn}, \text{Al}$ or P , and $\text{X} = \text{O}, \text{S}$ or Se) family of superionic conductors. *Energy Environ Sci* 2013;6:148-56. DOI
86. Whiteley JM, Woo JH, Hu E, Nam K, Lee S. Empowering the lithium metal battery through a silicon-based superionic conductor. *J Electrochem Soc* 2014;161:A1812-7. DOI
87. Hori S, Taminato S, Suzuki K, Hirayama M, Kato Y, Kanno R. Structure-property relationships in lithium superionic conductors having a $\text{Li}_{10}\text{GeP}_2\text{S}_{12}$ -type structure. *Acta Crystallogr B Struct Sci Cryst Eng Mater* 2015;71:727-36. DOI PubMed

88. Deiseroth H, Kong S, Eckert H, et al. $\text{Li}_6\text{PS}_5\text{X}$: a class of crystalline Li-rich solids with an unusually high Li^+ mobility. *Angew Chem* 2008;120:767-70. [DOI](#) [PubMed](#)
89. Gaudin E, Boucher F, Petricek VV, Taulelle F, Evain M. Structures and phase transitions of the A_7PSe_6 ($\text{A} = \text{Ag}, \text{Cu}$) argyrodite-type ionic conductors. II. Beta- and gamma- Cu_7PSe_6 . *Acta Crystallogr B* 2000;56:402-8. [DOI](#) [PubMed](#)
90. Kraft MA, Culver SP, Calderon M, et al. Influence of lattice polarizability on the ionic conductivity in the lithium superionic argyrodites $\text{Li}_6\text{PS}_5\text{X}$ ($\text{X} = \text{Cl}, \text{Br}, \text{I}$). *J Am Chem Soc* 2017;139:10909-18. [DOI](#) [PubMed](#)
91. Klerk NJJ, Rosłon I, Wagemaker M. Diffusion mechanism of Li Argyrodite solid electrolytes for Li-ion batteries and prediction of optimized halogen doping: the effect of Li vacancies, halogens, and halogen disorder. *Chem Mater* 2016;28:7955-63. [DOI](#)
92. Rao RP, Adams S. Studies of lithium argyrodite solid electrolytes for all-solid-state batteries: studies of lithium argyrodite solid electrolytes. *Phys Status Solidi A* 2011;208:1804-7. [DOI](#)
93. Hanghofer I, Brinek M, Eisbacher SL, et al. Substitutional disorder: structure and ion dynamics of the argyrodites $\text{Li}_6\text{PS}_5\text{Cl}$, $\text{Li}_6\text{PS}_5\text{Br}$ and $\text{Li}_6\text{PS}_5\text{I}$. *Phys Chem Chem Phys* 2019;21:8489-507. [DOI](#) [PubMed](#)
94. Chen HM, Maohua C, Adams S. Stability and ionic mobility in argyrodite-related lithium-ion solid electrolytes. *Phys Chem Chem Phys* 2015;17:16494-506. [DOI](#) [PubMed](#)
95. Morgan BJ. Mechanistic origin of superionic lithium diffusion in anion-disordered $\text{Li}_6\text{PS}_5\text{X}$ argyrodites. *Chem Mater* 2021;33:2004-18. [DOI](#) [PubMed](#) [PMC](#)
96. Kraft MA, Ohno S, Zinkevich T, et al. Inducing high ionic conductivity in the lithium superionic argyrodites $\text{Li}_{6+x}\text{P}_{1-x}\text{Ge}_x\text{S}_5$ for all-solid-state batteries. *J Am Chem Soc* 2018;140:16330-9. [DOI](#)
97. Minafra N, Culver SP, Krauskopf T, Senyshyn A, Zeier WG. Effect of Si substitution on the structural and transport properties of superionic Li-argyrodites. *J Mater Chem A* 2018;6:645-51. [DOI](#)
98. Wang P, Liu H, Patel S, et al. Fast ion conduction and its origin in $\text{Li}_{6-x}\text{PS}_{5-x}\text{Br}_{1+x}$. *Chem Mater* 2020;32:3833-40. [DOI](#)
99. Feng X, Chien P, Wang Y, et al. Enhanced ion conduction by enforcing structural disorder in Li-deficient argyrodites $\text{Li}_{6-x}\text{PS}_{5-x}\text{Cl}_{1+x}$. *Energy Stor Mater* 2020;30:67-73. [DOI](#)
100. Brinek M, Hiebl C, Wilkening HMR. Understanding the origin of enhanced Li-ion transport in nanocrystalline argyrodite-type Li_6PS_5 . *I. Chem Mater* 2020;32:4754-66. [DOI](#) [PubMed](#) [PMC](#)
101. Sun Y, Suzuki K, Hara K, et al. Oxygen substitution effects in $\text{Li}_{10}\text{GeP}_2\text{S}_{12}$ solid electrolyte. *J Power Sources* 2016;324:798-803. [DOI](#)
102. Bai Y, Zhao Y, Li W, Meng L, Bai Y, Chen G. New Insight for solid sulfide electrolytes LSiPSI by using Si/P/S as the raw materials and I doping. *ACS Sustainable Chem Eng* 2019;7:12930-7. [DOI](#)
103. Han F, Zhu Y, He X, Mo Y, Wang C. Electrochemical stability of $\text{Li}_{10}\text{GeP}_2\text{S}_{12}$ and $\text{Li}_7\text{La}_3\text{Zr}_2\text{O}_{12}$ solid electrolytes. *Adv Energy Mater* 2016;6:1501590. [DOI](#)
104. Han F, Gao T, Zhu Y, Gaskell KJ, Wang C. A battery made from a single material. *Adv Mater* 2015;27:3473-83. [DOI](#) [PubMed](#)
105. Richards WD, Miara LJ, Wang Y, Kim JC, Ceder G. Interface stability in solid-state batteries. *Chem Mater* 2016;28:266-73. [DOI](#)
106. Zhu Y, He X, Mo Y. Origin of outstanding stability in the lithium solid electrolyte materials: insights from thermodynamic analyses based on first-principles calculations. *ACS Appl Mater Interfaces* 2015;7:23685-93. [DOI](#) [PubMed](#)
107. Zhang Z, Zhang L, Liu Y, et al. Synthesis and characterization of argyrodite solid electrolytes for all-solid-state Li-ion batteries. *J Alloys Compounds* 2018;747:227-35. [DOI](#)
108. Muramatsu H, Hayashi A, Ohtomo T, Hama S, Tatsumisago M. Structural change of $\text{Li}_2\text{S}-\text{P}_2\text{S}_5$ sulfide solid electrolytes in the atmosphere. *Solid State Ionics* 2011;182:116-9. [DOI](#)
109. Hayashi A, Muramatsu H, Ohtomo T, Hama S, Tatsumisago M. Improved chemical stability and cyclability in $\text{Li}_2\text{S}-\text{P}_2\text{S}_5-\text{P}_2\text{O}_5-\text{ZnO}$ composite electrolytes for all-solid-state rechargeable lithium batteries. *J Alloys Compounds* 2014;591:247-50. [DOI](#)
110. Xu K. Electrolytes and interphases in Li-ion batteries and beyond. *Chem Rev* 2014;114:11503-618. [DOI](#) [PubMed](#)
111. Xiao Y, Wang Y, Bo S, Kim JC, Miara LJ, Ceder G. Understanding interface stability in solid-state batteries. *Nat Rev Mater* 2020;5:105-26. [DOI](#)
112. Famprakis T, Canepa P, Dawson JA, Islam MS, Masquelier C. Fundamentals of inorganic solid-state electrolytes for batteries. *Nat Mater* 2019;18:1278-91. [DOI](#) [PubMed](#)
113. Chen B, Ju J, Ma J, et al. An insight into intrinsic interfacial properties between Li metals and $\text{Li}_{10}\text{GeP}_2\text{S}_{12}$ solid electrolytes. *Phys Chem Chem Phys* 2017;19:31436-42. [DOI](#) [PubMed](#)
114. Swamy T, Park R, Sheldon BW, et al. Lithium metal penetration induced by electrodeposition through solid electrolytes: example in single-crystal $\text{Li}_6\text{La}_3\text{ZrTaO}_{12}$ garnet. *J Electrochem Soc* 2018;165:A3648-55. [DOI](#)
115. Nagao M, Hayashi A, Tatsumisago M, Kanetsuku T, Tsuda T, Kuwabata S. In situ SEM study of a lithium deposition and dissolution mechanism in a bulk-type solid-state cell with a $\text{Li}_2\text{S}-\text{P}_2\text{S}_5$ solid electrolyte. *Phys Chem Chem Phys* 2013;15:18600-6. [DOI](#) [PubMed](#)
116. Kasemchainan J, Zekoll S, Spencer Jolly D, et al. Critical stripping current leads to dendrite formation on plating in lithium anode solid electrolyte cells. *Nat Mater* 2019;18:1105-11. [DOI](#) [PubMed](#)
117. Wenzel S, Leichtweiss T, Krüger D, Sann J, Janek J. Interphase formation on lithium solid electrolytes - an in situ approach to study interfacial reactions by photoelectron spectroscopy. *Solid State Ionics* 2015;278:98-105. [DOI](#)
118. Wenzel S, Randau S, Leichtweiss T, et al. Direct observation of the interfacial instability of the fast ionic conductor $\text{Li}_{10}\text{GeP}_2\text{S}_{12}$ at the lithium metal anode. *Chem Mater* 2016;28:2400-7. [DOI](#)
119. Zhang L, Yang T, Du C, et al. Lithium whisker growth and stress generation in an in situ atomic force microscope-environmental transmission electron microscope set-up. *Nat Nanotechnol* 2020;15:94-8. [DOI](#) [PubMed](#)
120. Hagopian A, Doublet M, Filhol J. Thermodynamic origin of dendrite growth in metal anode batteries. *Energy Environ Sci*

- 2020;13:5186-97. [DOI](#)
121. Fan X, Ji X, Han F, et al. Fluorinated solid electrolyte interphase enables highly reversible solid-state Li metal battery. *Sci Adv* 2018;4:eaau9245. [DOI](#) [PubMed](#) [PMC](#)
122. Kazyak E, Garcia-mendez R, Lepage WS, et al. Li penetration in ceramic solid electrolytes: operando microscopy analysis of morphology, propagation, and reversibility. *Matter* 2020;2:1025-48. [DOI](#)
123. Liu H, Cheng X, Huang J, et al. Controlling dendrite growth in solid-state electrolytes. *ACS Energy Lett* 2020;5:833-43. [DOI](#)
124. Shen F, Dixit MB, Xiao X, Hatzell KB. Effect of Pore connectivity on Li dendrite propagation within LLZO electrolytes observed with synchrotron X-ray tomography. *ACS Energy Lett* 2018;3:1056-61. [DOI](#)
125. Han F, Westover AS, Yue J, et al. High electronic conductivity as the origin of lithium dendrite formation within solid electrolytes. *Nat Energy* 2019;4:187-96. [DOI](#)
126. Brissot C, Rosso M, Chazalviel JN, Lascaud S. Dendritic growth mechanisms in lithiumrpolymer cells. *J Power Sources* 1999;81-82:925-9. [DOI](#)
127. Cao L, Gao X, Zhang B, Ou X, Zhang J, Luo WB. Bimetallic sulfide $\text{Sb}_2\text{S}_3@\text{FeS}_2$ hollow nanorods as high-performance anode materials for sodium-ion batteries. *ACS Nano* 2020;14:3610-20. [DOI](#) [PubMed](#)
128. Wang L, Zhou Z, Yan X, et al. Engineering of lithium-metal anodes towards a safe and stable battery. *Energy Stor Mater* 2018;14:22-48. [DOI](#)
129. Li Y, Gu Q, Johannessen B, et al. Synergistic Pt doping and phase conversion engineering in two-dimensional MoS_2 for efficient hydrogen evolution. *Nano Energy* 2021;84:105898. [DOI](#)
130. Zhao C, Zhao B, Yan C, et al. Liquid phase therapy to solid electrolyte-electrode interface in solid-state Li metal batteries: a review. *Energy Stor Mater* 2020;24:75-84. [DOI](#)
131. Zhang JG, Xu W, Xiao J, Cao X, Liu J. Lithium metal anodes with nonaqueous electrolytes. *Chem Rev* 2020;120:13312-48. [DOI](#) [PubMed](#)
132. Park KH, Bai Q, Kim DH, et al. Design strategies, practical considerations, and new solution processes of sulfide solid electrolytes for all-solid-state batteries. *Adv Energy Mater* 2018;8:1800035. [DOI](#)
133. Taklu BW, Su W, Nikodimos Y, et al. Dual CuCl doped argyrodite superconductor to boost the interfacial compatibility and air stability for all solid-state lithium metal batteries. *Nano Energy* 2021;90:106542. [DOI](#)
134. Zhao F, Sun Q, Yu C, et al. Ultrastable anode interface achieved by fluorinating electrolytes for all-solid-state Li metal batteries. *ACS Energy Lett* 2020;5:1035-43. [DOI](#)
135. Han F, Yue J, Zhu X, Wang C. Suppressing Li dendrite formation in $\text{Li}_2\text{S}-\text{P}_2\text{S}_5$ solid electrolyte by LiI incorporation. *Adv Energy Mater* 2018;8:1703644. [DOI](#)
136. Su Y, Ye L, Fitzhugh W, et al. A more stable lithium anode by mechanical constriction for solid state batteries. *Energy Environ Sci* 2020;13:908-16. [DOI](#)
137. Ji X, Hou S, Wang P, et al. Solid-state electrolyte design for lithium dendrite suppression. *Adv Mater* 2020;32:e2002741. [DOI](#) [PubMed](#)
138. Wan H, Liu S, Deng T, et al. Bifunctional interphase-enabled $\text{Li}_{10}\text{GeP}_2\text{S}_{12}$ electrolytes for lithium-sulfur battery. *ACS Energy Lett* 2021;6:862-8. [DOI](#)
139. Peng J, Wu D, Song F, et al. High current density and long cycle life enabled by sulfide solid electrolyte and dendrite-free liquid lithium anode. *Adv Funct Materials* 2022;32:2105776. [DOI](#)
140. Ye L, Li X. A dynamic stability design strategy for lithium metal solid state batteries. *Nature* 2021;593:218-22. [DOI](#) [PubMed](#)
141. Wang Z, Jiang Y, Wu J, et al. Doping effects of metal cation on sulfide solid electrolyte/lithium metal interface. *Nano Energy* 2021;84:105906. [DOI](#)
142. Zhao R, Kmiec S, Hu G, Martin SW. Lithium thiosilicophosphate glassy solid electrolytes synthesized by high-energy ball-milling and melt-quenching: improved suppression of lithium dendrite growth by Si doping. *ACS Appl Mater Interfaces* 2020;12:2327-37. [DOI](#) [PubMed](#)
143. Zhang Z, Zhang L, Yan X, et al. All-in-one improvement toward $\text{Li}_6\text{PS}_5\text{Br}$ -based solid electrolytes triggered by compositional tune. *J Power Sources* 2019;410-411:162-70. [DOI](#)
144. Liu G, Weng W, Zhang Z, Wu L, Yang J, Yao X. Densified $\text{Li}_6\text{PS}_5\text{Cl}$ nanorods with high ionic conductivity and improved critical current density for all-solid-state lithium batteries. *Nano Lett* 2020;20:6660-5. [DOI](#) [PubMed](#)
145. Zhao Q, Stalin S, Zhao C, Archer LA. Designing solid-state electrolytes for safe, energy-dense batteries. *Nat Rev Mater* 2020;5:229-52. [DOI](#)
146. Zhu Y, He X, Mo Y. First principles study on electrochemical and chemical stability of solid electrolyte-electrode interfaces in all-solid-state Li-ion batteries. *J Mater Chem A* 2016;4:3253-66. [DOI](#)
147. Lepley ND, Holzwarth NAW. Modeling interfaces between solids: application to Li battery materials. *Phys Rev B* 2015;92:214201. [DOI](#)
148. Peng Z, Zhao N, Zhang Z, et al. Stabilizing Li/electrolyte interface with a transplantable protective layer based on nanoscale LiF domains. *Nano Energy* 2017;39:662-72. [DOI](#)
149. Sakuma M, Suzuki K, Hirayama M, Kanno R. Reactions at the electrode/electrolyte interface of all-solid-state lithium batteries incorporating Li-M (M = Sn, Si) alloy electrodes and sulfide-based solid electrolytes. *Solid State Ionics* 2016;285:101-5. [DOI](#)
150. Liang X, Pang Q, Kochetkov IR, et al. A facile surface chemistry route to a stabilized lithium metal anode. *Nat Energy* 2017;2:17119. [DOI](#)
151. Santhosha AL, Medenbach L, Buchheim JR, Adelhelm P. The Indium-lithium electrode in solid-state lithium-ion batteries: phase

- formation, redox potentials, and interface stability. *Batteries Supercaps* 2019;2:524-9. DOI
152. Il'ina EA, Lylin ED, Plekhanov MS. Investigation of Li-In alloy application as anode for all-solid-state batteries. *J Phys Conf Ser* 2021;1967:012012. DOI
153. Nagao M, Hayashi A, Tatsumisago M. Bulk-type lithium metal secondary battery with indium thin layer at interface between Li electrode and $\text{Li}_2\text{S}-\text{P}_2\text{S}_5$ solid electrolyte. *Electrochemistry* 2012;80:734-6. DOI
154. Lee Y, Fujiki S, Jung C, et al. High-energy long-cycling all-solid-state lithium metal batteries enabled by silver-carbon composite anodes. *Nat Energy* 2020;5:299-308. DOI
155. Tan DHS, Chen YT, Yang H, et al. Carbon-free high-loading silicon anodes enabled by sulfide solid electrolytes. *Science* 2021;373:1494-9. DOI PubMed
156. Choi HJ, Kang DW, Park JW, et al. In situ formed Ag-Li intermetallic layer for stable cycling of all-solid-state lithium batteries. *Adv Sci (Weinh)* 2022;9:e2103826. DOI PubMed PMC
157. Yamada Y, Wang J, Ko S, Watanabe E, Yamada A. Advances and issues in developing salt-concentrated battery electrolytes. *Nat Energy* 2019;4:269-80. DOI
158. Zhang Z, Chen S, Yang J, et al. Interface re-engineering of $\text{Li}_{10}\text{GeP}_2\text{S}_{12}$ electrolyte and lithium anode for all-solid-state lithium batteries with ultralong cycle life. *ACS Appl Mater Interfaces* 2018;10:2556-65. DOI PubMed
159. Liang J, Li X, Zhao Y, et al. An air-stable and dendrite-free Li anode for highly stable all-solid-state sulfide-based Li batteries. *Adv Energy Mater* 2019;9:1902125. DOI
160. Yang M, Liu Y, Nolan AM, Mo Y. Interfacial atomistic mechanisms of lithium metal stripping and plating in solid-state batteries. *Adv Mater* 2021;33:e2008081. DOI PubMed
161. Chen Y, Li W, Sun C, et al. Sustained release-driven formation of ultrastable SEI between $\text{Li}_6\text{PS}_5\text{Cl}$ and lithium anode for sulfide-based solid-state batteries. *Adv Energy Mater* 2021;11:2002545. DOI
162. Li J, Su H, Li M, et al. Fluorinated interface layer with embedded zinc nanoparticles for stable lithium-metal anodes. *ACS Appl Mater Interfaces* 2021;13:17690-8. DOI PubMed
163. Klerk NJJ, Wagelmaker M. Space-charge layers in all-solid-state batteries; important or negligible? *ACS Appl Energy Mater* 2018;1:5609-18. DOI PubMed PMC
164. Yu C, Ganapathy S, de Klerk NJ, et al. Unravelling Li-ion transport from picoseconds to seconds: bulk versus interfaces in an argyrodite $\text{Li}_6\text{PS}_5\text{Cl}-\text{Li}_2\text{S}$ all-solid-state Li-ion battery. *J Am Chem Soc* 2016;138:11192-201. DOI PubMed
165. Wang L, Xie R, Chen B, et al. In-situ visualization of the space-charge-layer effect on interfacial lithium-ion transport in all-solid-state batteries. *Nat Commun* 2020;11:5889. DOI PubMed PMC
166. Yu C, Ganapathy S, Eck ERHV, et al. Accessing the bottleneck in all-solid state batteries, lithium-ion transport over the solid-electrolyte-electrode interface. *Nat Commun* 2017;8:1086. DOI PubMed PMC
167. Walther F, Koerver R, Fuchs T, et al. Visualization of the interfacial decomposition of composite cathodes in argyrodite-based all-solid-state batteries using time-of-flight secondary-ion mass spectrometry. *Chem Mater* 2019;31:3745-55. DOI
168. Koerver R, Aygün I, Leichtweiß T, et al. Capacity fade in solid-state batteries: interphase formation and chemomechanical processes in nickel-rich layered oxide cathodes and lithium thiophosphate solid electrolytes. *Chem Mater* 2017;29:5574-82. DOI
169. Zhang J, Zheng C, Li L, et al. Unraveling the intra and intercycle interfacial evolution of $\text{Li}_6\text{PS}_5\text{Cl}$ -based all-solid-state lithium batteries. *Adv Energy Mater* 2020;10:1903311. DOI
170. Auvergniot J, Cassel A, Ledueil J, Viallet V, Seznec V, Dedryvère R. Interface stability of argyrodite $\text{Li}_6\text{PS}_5\text{Cl}$ toward LiCoO_2 , $\text{LiNi}_{1/3}\text{Co}_{1/3}\text{Mn}_{1/3}\text{O}_2$, and LiMn_2O_4 in bulk all-solid-state batteries. *Chem Mater* 2017;29:3883-90. DOI
171. Zheng B, Liu X, Zhu J, et al. Unraveling (electro)-chemical stability and interfacial reactions of $\text{Li}_{10}\text{SnP}_2\text{S}_{12}$ in all-solid-state Li batteries. *Nano Energy* 2020;67:104252. DOI
172. Zhang W, Leichtweiß T, Culver SP, et al. The detrimental effects of carbon additives in $\text{Li}_{10}\text{GeP}_2\text{S}_{12}$ -based solid-state batteries. *ACS Appl Mater Interfaces* 2017;9:35888-96. DOI PubMed
173. Liu X, Zheng B, Zhao J, et al. Electrochemo-mechanical effects on structural integrity of Ni-rich cathodes with different microstructures in all solid-state batteries. *Adv Energy Mater* 2021;11:2003583. DOI
174. Ohno S, Koerver R, Dewald G, et al. Observation of chemomechanical failure and the influence of cutoff potentials in all-solid-state Li-S batteries. *Chem Mater* 2019;31:2930-40. DOI
175. Wang S, Zhang W, Chen X, et al. Influence of crystallinity of lithium thiophosphate solid electrolytes on the performance of solid-state batteries. *Adv Energy Mater* 2021;11:2100654. DOI
176. Minnmann P, Quillman L, Burkhardt S, Richter FH, Janek J. Editors' choice-quantifying the impact of charge transport bottlenecks in composite cathodes of all-solid-state batteries. *J Electrochem Soc* 2021;168:040537. DOI
177. Li X, Jin L, Song D, et al. LiNbO_3 -coated $\text{LiNi}_{0.8}\text{Co}_{0.1}\text{Mn}_{0.1}\text{O}_2$ cathode with high discharge capacity and rate performance for all-solid-state lithium battery. *J Energy Chem* 2020;40:39-45. DOI
178. Peng L, Ren H, Zhang J, et al. LiNbO_3 -coated $\text{LiNi}_{0.7}\text{Co}_{0.1}\text{Mn}_{0.2}\text{O}_2$ and chlorine-rich argyrodite enabling high-performance solid-state batteries under different temperatures. *Energy Stor Mater* 2021;43:53-61. DOI
179. Banerjee A, Tang H, Wang X, et al. Revealing nanoscale solid-solid interfacial phenomena for long-life and high-energy all-solid-state batteries. *ACS Appl Mater Interfaces* 2019;11:43138-45. DOI PubMed
180. Li X, Jiang Z, Cai D, et al. Single-crystal-layered Ni-rich oxide modified by phosphate coating boosting interfacial stability of $\text{Li}_{10}\text{SnP}_2\text{S}_{12}$ -based all-solid-state Li batteries. *Small* 2021;17:e2103830. DOI PubMed
181. Wang Y, Lv Y, Su Y, Chen L, Li H, Wu F. 5V-class sulfurized spinel cathode stable in sulfide all-solid-state batteries. *Nano Energy* 2021;90:106589. DOI

182. Randau S, Weber DA, Kötz O, et al. Benchmarking the performance of all-solid-state lithium batteries. *Nat Energy* 2020;5:259-70. [DOI](#)
183. Wang S, Zhang X, Liu S, et al. High-conductivity free-standing $\text{Li}_0\text{PS}_5\text{Cl}$ /poly(vinylidene difluoride) composite solid electrolyte membranes for lithium-ion batteries. *J Materomics* 2020;6:70-6. [DOI](#)
184. Liu G, Shi J, Zhu M, et al. Ultra-thin free-standing sulfide solid electrolyte film for cell-level high energy density all-solid-state lithium batteries. *Energy Stor Mater* 2021;38:249-54. [DOI](#)
185. Zhu G, Zhao C, Peng H, et al. A self-limited free-standing sulfide electrolyte thin film for all-solid-state lithium metal batteries. *Adv Funct Mater* 2021;31:2101985. [DOI](#)
186. Zhang Z, Wu L, Zhou D, Weng W, Yao X. Flexible sulfide electrolyte thin membrane with ultrahigh ionic conductivity for all-solid-state lithium batteries. *Nano Lett* 2021;21:5233-9. [DOI](#) [PubMed](#)
187. Xu J, Li Y, Lu P, et al. Water-stable sulfide solid electrolyte membranes directly applicable in all-solid-state batteries enabled by superhydrophobic Li^+ -conducting protection layer. *Adv Energy Mater* 2022;12:2102348. [DOI](#)